J. Appl. Comput. Mech., 11(3) (2025) 585-610
DOI: 10.22055/jacm.2024.46918.4625

ISSN: 2383-4536
jacm.scu.ac.ir

Shahid Chamran
University of Ahvaz

Journal of
Applied and Computational Mechanics

Research Paper

CAS Wavelet Based Numerical Technique for the Solution of Dusty Tangent Hyperbolic Fluid Flow with Magnetic Dipole Effect, Quadratic Convection and Entropy Generation

S.C. Shiralashetti[1], Priyanka I. Kulkarni[1], Savita I. Hanaji[2]

[1] Department of Mathematics, Karnatak University, Dharwad, 580003, Karnataka, India, Email: scshiralashetti@kud.ac.in (S.C.S.); priyankakulkarni42@gmail.com (P.I.K.)

[2] KLE Technological University, Dr. M. S. Sheshgiri College of Engineering and Technology, Udyambag, Belagavi, 590008, Karnataka, India, Email: savitahanaji@klescet.ac.in

Received May 15 2024; Revised August 21 2024; Accepted for publication September 19 2024.
Corresponding author: S.C. Shiralashetti (scshiralashetti@kud.ac.in)

Abstract. This paper presents the CAS wavelet based numerical technique for the solution of non-linear system of differential equations arising in the analysis of an unsteady dusty tangent hyperbolic fluid flow over a stretching sheet through porous medium with magnetic dipole effect, quadratic convection, non-linear radiation, convective boundary and entropy generation. Initially, the proposed method is implemented on the test problem having the exact solution. The results obtained are very close to the exact solution in comparison with the Runge-Kutta Fehlberg 4^{th} – 5^{th} order method. The considered dusty fluid problem is solved by using the proposed technique. The solutions obtained for certain fixed parameters are compared and found to be coinciding with the solutions given in the literature. The comparisons and convergence analysis validate the method. The flow behaviour of dusty tangent hyperbolic fluid is analysed and the impact of various factors on the velocity and thermal profile of the fluid are studied. It is inferred that the Weissenberg number, power law index and Ferro-hydrodynamic interaction parameter declines the velocity and improves the temperature. Opposite behaviour is observed for mixed convection and quadratic convection parameters. The temperature increases for the Biot number. The Weissenberg number declines the entropy generation and enhances the Bejan number. A reverse trend is noticed for Brinkman number. CAS wavelet based numerical technique is simple, reliable, highly accurate, efficient and effective tool to solve the non-linear system of differential equations arising in dusty fluid flow problems.

Keywords: CAS wavelets, Operational matrix, Dusty tangent hyperbolic fluid, Magnetic dipole, Entropy generation.

1. Introduction

Dusty fluids are the fluids consisting of suspension of solid dust particles. The suspension of solid dust particles in the fluid improves the thermal conductivity of the fluid which enhances the heat transfer. Dusty fluids are used in many applications like wastewater treatment, fluidization, vehicle smoke emissions, crude oil purification, power plant pipework, petroleum industry, caustic particulate matter in mining, nuclear reactor cooling and many other. The fundamental research of dusty fluid was pioneered by Saffman [1]. Since then, numerous investigations have been carried out on dusty fluids. Shiralashetti et al. [2] analysed the Darcy–Forchheimer flow of Erying–Powell radiated dusty fluid over a stretching sheet with Cattaneo–Christov heat flux. Sulochana et al. [3] studied dusty nanofluid flow with non-uniform heat source/sink. Almaneea [4] studied heat transfer through a dusty Carreau fluid with nanoparticles. Dey et al. [5] investigated the hydromagnetic flow of dusty fluid over a stretching curved surface. Upadhya et al. [6] analysed Eyring-Powell dusty fluid flow in a deferment of aluminium and ferrous oxide nanoparticles with and Cattaneo-Christov heat flux. Krishnamurthy et al. [7] studied the suspended particle effect on slip flow and melting heat transfer of nanofluid with nonlinear thermal radiation.

A fluid that disobeys the Newton's law of viscosity is referred to as non-Newtonian fluid. Non-Newtonian fluids find its applications in numerous engineering and industrial processes including fermentation, food mixing, guided missiles, heavy oils, blood flow, lubrications, etc. Tangent hyperbolic fluid is one of the interesting non-Newtonian models derived from the kinetic theory of liquids which can explain the effects of shear thinning more accurately than any other model and adheres to the power law model. Akbar et al. [8] analysed the magneto hydrodynamic boundary layer flow of tangent hyperbolic fluid with magnetic field. Ullah et al. [9] investigated the Magnetohydrodynamic tangent hyperbolic fluid flow. Sreenivasulu et al. [10] analysed an inclined Lorentzian force effect on tangent hyperbolic radiative slip flow imbedded carbon nanotubes: Lie group analysis. Zeb et al. [11] investigated Lie group analysis of double diffusive MHD tangent hyperbolic fluid flow. Moatimid et al. [12] studied the tangent-hyperbolic micropolar nanofluid flow over an extending layer.

Published online: September 23 2024

A magnetic dipole is an arrangement of two magnetic charges of same strength and opposite sign that are spaced apart by a minimal distance. The magnetic dipole phenomenon is useful in a number of heat transfer applications, including drug delivery systems, NMR spectroscopy, electronic circuits, magnotherapy, hyperthermia treatments, additive manufacturing, etc. Ferrofluids characterize a special class of magnetizable fluid that attract to the magnetic poles. These fluids are smart fluid materials carries colloidal suspended magnetic nanoparticles (ferromagnetic or ferrimagnetic particles) and whose properties can be altered by applying an external magnetic field. The purpose of using the ferrofluids is to induce the effective magnetic dipole moments in the system. Ferrofluids are used in different smart appliances such as semiconductor processing, food preserving, X-ray machine, aerodynamics, crystal processing, cooling agent, nuclear power plants, computer peripherals and metal spinning, fibre optics, heat treating furnace, robotics, drawing plastic, avionics, etc. Due to the wide range of applications, numerous researchers have recently shown a strong desire to investigate the magnetic dipole effect and heat transfer on ferrofluid flow under different physical aspects. Andersson and Valnes [13] investigated the ferrofluid flow over a stretching sheet in the presence of a magnetic dipole. Majeed et al. [14] boundary layer Maxwell Ferro-fluid flow under magnetic dipole with Soret and suction effects. Nidhi and Kumar [15] analysed the magnetic dipole and mixed convective effect on boundary layer flow of ferromagnetic micropolar hybrid nanofluid. Kamis et al. [16] studied the magnetic dipole effect on hybrid ferrofluid on an inclined stretching sheet. Tijani et al. [17] analysed the magnetic dipole effect on Reiner-Philippoff boundary layer flow. Imtiaz et al. [18] investigated the magnetic dipole impact on nanofluid flow characteristics over a stretching sheet.

In many thermal applications such as combustions, plastic manufacturing, heat storage systems, solar collectors, polymers industries, heat exchangers, nuclear reactors, etc., the temperature gradient is substantially large. Hence, the density varies non-linearly with temperature. This affects the flow behaviour significantly. The non-linearities and small-scale movements are taken into consideration by quadratic term. Thus, the more accurate representation of fluid flow behaviour can be achieved by considering the quadratic term. Goren [19] initially investigated the quadratic convection. Obalalu et al. [20] analysed energy optimization of quadratic thermal convection on two-phase boundary layer flow. Abbas et al. [21] studied the thermal Marangoni convection in two-phase quadratic convective flow of dusty MHD trihybrid nanofluid with non-linear heat source. Jiann et al. [22] analysed the quadratic mixed convection MHD Carreau fluid flow on cylinder.

Boundary conditions such as a predetermined temperature or a specific heat flux at the surface are commonly employed in the modelling of boundary layer flow problems. On the other hand, there are the problems in which the surface temperature affects surface heat transmission. Such situation occurs when there is Newtonian heating of the convective fluid from the surface. The study of convective heat flow attracted many researchers due to the extensive industry requirement such as nuclear reactors, gas turbines, geothermal energy extraction, etc. Imran et al. [23] investigated the bioconvective Maxwell nanofluid flow with nield/convective boundary constraints. Venkatesh et al. [24] studied the effects of thermal radiation, convective boundary condition and induced magnetic field on MHD Maxwell fluid with nanoparticles. Shah et al. [25] studied the thermal radiation effect on Carreau fluid with convective boundary condition. Raje et al. [26] studied entropy analysis of the MHD Jeffrey fluid flow with convective boundaries.

In recent years, the study of entropy generation has drawn the focus of numerous researchers. Entropy generation represents an irreversible energy dissipation in the thermal system due to heat transfer, viscous dissipation, magnetic field, buoyancy and many other factors. Thus, the study of entropy generation is essential to analyse and manage the efficiency of the thermal system. Entropy generation optimization is useful in various systems such as heat exchangers, air separators, reactors, pumps, microchannels, electronic cooling systems etc. Bejan [27] analysed the entropy generation minimization. Reddy et al. [28] analysed the entropy generation and activation energy on a Carreau–Yasuda nanofluid flow. Wang et al. [29] studied the entropy generation in nanofluid flow with thermal radiation applications. Hayat et al. [30] analysed Entropy generation optimization in nanofluid flow by variable thick sheet.

Wavelet theory has drawn a lot of interest recently due to its potent uses in a various fields including optimal control, numerical analysis, nonlinear dynamics and many others. Wavelets have several advantageous features like orthogonality, vanishing moment, arbitrary regularity and compact support due to which wavelet technique is powerful and efficient for the numerical approximation of the function. Several wavelet techniques have been implemented to solve differential and integral equations in the literature, including the following: Haar wavelets [31, 32], Chebyshev wavelets [33], Legendre wavelets [34], Jacobi wavelets [35], Chelyshkov wavelets [2], Fibonacci wavelets [36] and many others.

Cosine and Sine (CAS) wavelets is one of the wavelet families that enables to more effectively approximate arbitrary functions, even ones that exhibit discontinuity. CAS wavelets are introduced by Yousefi and Banifatemi [37] for the numerical solution of Fredholm integral equations. Danfu and Xufeng [38] introduced CAS wavelet operation matrix of integration to solve integro-differential equations. Furthermore, the CAS wavelets have been used to solve the fractional integro-differential equations [39], Volterra-integro-differential equations [40], boundary integral equations [41], Caputo–Hadamard fractional differential equation [42], Caputo fractional differential equations [43], stochastic Itô-Volterra integral equations [44]. As per the literature review, the CAS wavelet method is used to solve different types of differential and integral equations but it is less concentrated on the application point of view. To the best of our knowledge, most of the researchers are used different wavelets to analyse the fluid flow problems rather than CAS wavelets method. We have focused on developing the CAS wavelet method to solve the system of non-linear ordinary differential equations (ODEs) that arise in the analysis of flow behaviour and heat transfer of a dusty fluid problem. Which will be helpful to solve most of the industrial and engineering problem with the high accuracy.

In this paper, we have developed CAS wavelet based numerical technique (CASWBNT) for the numerical solution of typical non-linear system of ordinary differential equations (ODEs) arising in the study of an unsteady dusty tangent hyperbolic fluid flow over a stretching sheet through porous medium with magnetic dipole effect, quadratic convection, convection boundary, non-linear radiation and entropy generation. The novelty and research gap between the literature review [13 - 18, 20 - 22] and the present study is, the effect of magnetic dipole and quadratic convection has been analysed separately for different fluids like nanofluid, Maxwell fluid, hybrid nanofluid, micropolar hybrid nanofluid, Reiner-Philippoff fluid, trihybrid nanofluid, Carreau fluid, dusty MHD trihybrid nanofluid in steady state in the literature [13-18, 20-22], but none has investigated the combined effects of magnetic dipole and quadratic convection for an unsteady dusty tangent hyperbolic fluid flow to the best of our knowledge. Additional factors contributing to the uniqueness of the problem are non-linear radiation, convective boundary and entropy generation analysis. Moreover, we have developed CASWBNT for the solution of non-linear system of ODEs to analyse the considered dusty fluid flow problem.

The following research questions explains the objective and necessity of the present problem:

a) What are the impacts of fluid parameters: Weissenberg number and power law index on velocity and thermal attribute of fluid and dust phase?
b) How does Ferro-hydrodynamic interaction parameter affect the velocity and thermal profile of dusty tangent hyperbolic fluid?
c) What is the effect of quadratic convection on velocity and temperature of dusty tangent hyperbolic fluid?

d) What is the influence of unsteady parameter, Fluid-particle interaction parameter and porosity parameter on the velocity and temperature of fluid and dust phase?
e) How does nonlinear thermal radiation, Biot number, Eckert number, temperature ratio and Prandtl number impact the thermal profile?
f) How the increment of diverse parameters affects the skin-frictions coefficient and Nusselt number and what are their numerical outcomes?
g) What are the effects of the Weissenberg number, Brinkman number and Radiation parameter on entropy generation and Bejan number?

The presented model has numerous applications in fluid dynamics and advancement of heat transfer which focuses on unsteady dusty tangent hyperbolic fluid flow over a stretching sheet through porous medium with magnetic dipole effect, quadratic convection, convective boundary, non-linear radiation and entropy generation. The results of this model provide useful information to enhance thermal management strategies, thermal system efficiency and energy efficiency in many engineering, medical and industrial applications, including drug delivery systems, NMR spectroscopy, electronic circuits, magnotherapy, hyperthermia treatments, fibre optics, additive manufacturing, semiconductor processing, laser, sealing applications, robotics, food preserving, X-ray machine, aerodynamics, crystal processing, cooling agent, filtration, nuclear power plants, computer peripherals and metal spinning, loudspeakers, refrigeration, solar collectors, avionics, combustions, heat storage systems, textile machine tools, polymers industries, heat exchangers, material dying and many other.

2. Properties of CAS Wavelet

2.1. Wavelets and CAS Wavelets

Wavelets are collection of self-similar functions constructed by shifting and scaling of a mother wavelet. The family of continuous wavelets is obtained by varying continuously the scaling and shifting parameters ε and δ, respectively, and is defined as:

$$\psi_{\varepsilon,\delta}(\eta)=\frac{1}{\sqrt{|\varepsilon|}}\psi\left(\frac{\eta-\delta}{\varepsilon}\right),\quad \varepsilon,\delta\in\mathbb{R},\ \varepsilon\neq 0 \tag{1}$$

By limiting ε and δ in Eq. (1) to discrete values $\varepsilon=\varepsilon_0^{-k}$, $\delta=n\delta_0\varepsilon_0^{-k}$, $\varepsilon_0>1$, $\delta_0>0$ and $n,k\in\mathbb{N}$, we obtain the discrete wavelets family given as follows:

$$\psi_{k,n}(\eta)=|\varepsilon|^{\frac{k}{2}}\psi\left(\varepsilon_0^k\eta-n\delta_0\right)$$

In particular, when $\varepsilon_0=2$ and $\delta_0=1$ are chosen, $\psi_{k,n}(\eta)$ forms an orthonormal basis for $L^2(\mathbb{R})$:

$$\psi_{k,n}(\eta)=2^{\frac{k}{2}}\psi\left(2^k\eta-n\right)$$

For any non-negative integer k, the CAS wavelets on the interval $[0,L]$ is defined as [37, 38]:

$$w_{n,m}(\eta)=\begin{cases}2^{\frac{k}{2}}\ \mathrm{CAS}_m\left(\dfrac{2^k\eta}{L}-n\right) & \text{for } \dfrac{nL}{2^k}\le t\le\dfrac{(n+1)L}{2^k}\\ 0 & \text{otherwise}\end{cases} \tag{2}$$

where $\mathrm{CAS}_m(\eta)=\cos(2m\pi\eta)+\sin(2m\pi\eta)$, $m\in\mathbb{Z}$, $k\ge 0\in\mathbb{Z}$, $n=0,\ 1,\ 2,\ldots,\ 2^k-1$. The translation parameter is $\delta=nL/2^k$ and dilation parameter is $\varepsilon=L/2^k$.

We consider the collocation points $\eta_l=(l-0.5)L/N$, $l=1,2,\ldots,N$, where $N=2^k(2M+1)$.

2.2. Function approximation

Any function $f(\eta)$ which is square integrable over $[0,L]$ can be expressed in terms of CAS wavelets as follows:

$$f(\eta)=\sum_{n=0}^{\infty}\sum_{m\in\mathbb{Z}}a_{nm}w_{n,m}(\eta),\quad \eta\in[0,L] \tag{3}$$

where $w_{n,m}(\eta)$ are the CAS wavelet basis defined in Eq. (2) and a_{nm} are the CAS wavelet coefficients can be determined by the inner product:

$$a_{nm}=\ <f(\eta),w_{n,m}(\eta)> \tag{4}$$

For numerical purpose, we truncate the infinite series in Eq. (3) to finite series as follows:

$$f(\eta)=\sum_{n=0}^{2^k-1}\sum_{m=-M}^{M}a_{nm}w_{n,m}(\eta)=A^TW(\eta),\quad \eta\in[0,L] \tag{5}$$

where A is coefficient matrix of CAS wavelet and $W(\eta)$ is CAS wavelet matrix both are of order $N=2^k(2M+1)\times 1$ assumed as:

$$A^T=[a_{0\,(-M)},\ a_{0\,(-M+1)},\ldots,a_{0\,M},\ a_{1\,(-M)},\ldots,\ a_{1\,M},\ldots,\ a_{(2^k-1)\,(-M)},\ldots,\ a_{(2^k-1)\,M}] \tag{6a}$$

$$W(\eta)=\left[w_{0,(-M)}(\eta),\ w_{0,(-M+1)}(\eta),\ldots,w_{0,,(M)}(\eta),\ w_{1,(-M)}(\eta),\ w_{1,(-M+1)}(\eta),\ldots,w_{1,(M)}(\eta),\ldots,w_{(2^k-1),(-M)}(\eta),\ w_{(2^k-1),(-M+1)}(\eta),\ldots,w_{(2^k-1),(M)}(\eta)\right]^T \tag{6b}$$

where superscript T is the transpose of matrix.

2.3. CAS Wavelet integration operational matrices

In this section, we find CAS wavelet integration operational matrices that are crucial in dealing with the ODEs. First, we derive the integration operation matrix of order $N=6$ ($M=1$ and $k=1$). The six CAS wavelet basis are:

$$w_{0,(-1)}(\eta)=\begin{cases}\sqrt{2}\left(\cos\left(\frac{4\pi\eta}{L}\right)-\sin\left(\frac{4\pi\eta}{L}\right)\right) & 0\le\eta\le\frac{L}{2}\\ 0 & \text{otherwise}\end{cases}\tag{7a}$$

$$w_{0,0}(\eta)=\begin{cases}\sqrt{2} & 0\le\eta\le\frac{L}{2}\\ 0 & \text{otherwise}\end{cases}\tag{7b}$$

$$w_{0,1}(\eta)=\begin{cases}\sqrt{2}\left(\cos\left(\frac{4\pi\eta}{L}\right)+\sin\left(\frac{4\pi\eta}{L}\right)\right) & 0\le\eta\le\frac{L}{2}\\ 0 & \text{otherwise}\end{cases}\tag{7c}$$

$$w_{1,(-1)}(\eta)=\begin{cases}\sqrt{2}\left(\cos\left(2\pi\left(\left(\frac{2\pi\eta}{L}\right)-1\right)\right)-\sin\left(2\pi\left(\left(\frac{2\pi\eta}{L}\right)-1\right)\right)\right) & \frac{L}{2}\le\eta\le L\\ 0 & \text{otherwise}\end{cases}\tag{7d}$$

$$w_{1,0}(\eta)=\begin{cases}\sqrt{2} & \frac{L}{2}\le\eta\le L\\ 0 & \text{otherwise}\end{cases}\tag{7e}$$

$$w_{1,1}(\eta)=\begin{cases}\sqrt{2}\left(\cos\left(2\pi\left(\left(\frac{2\pi\eta}{L}\right)-1\right)\right)+\sin\left(2\pi\left(\left(\frac{2\pi\eta}{L}\right)-1\right)\right)\right) & \frac{L}{2}\le\eta\le L\\ 0 & \text{otherwise}\end{cases}\tag{7f}$$

Integrating the wavelet basis mentioned in Eq. (7) and then expressing as a linear combination of CAS wavelet basis using Eq. (4) [35, 38], we obtain the following:

$$\int_0^\eta w_{0,(-1)}(\eta)d\eta=\begin{cases}\frac{\sqrt{2}}{4\pi}\left(\cos(4\pi\eta/L)+\sin(4\pi\eta/L)-1\right) & 0\le\eta\le\frac{L}{2}\\ 0 & \frac{L}{2}\le\eta\le L\end{cases}$$

$$=-\frac{1}{4\pi}w_{0,0}(\eta)+\frac{1}{4\pi}w_{0,1}(\eta)=\left[0,\ -\frac{1}{4\pi},\ \frac{1}{4\pi},\ 0,\ 0,\ 0\right]W_6(\eta)$$

$$=-\frac{1}{4\pi}w_{0,0}(\eta)+\frac{1}{4\pi}w_{0,1}(\eta)=\left[0,\ -\frac{1}{4\pi},\ \frac{1}{4\pi},\ 0,\ 0,\ 0\right]W_6(\eta)$$

$$\int_0^\eta w_{0,0}(\eta)d\eta=\begin{cases}\sqrt{2}\eta & 0\le\eta\le\frac{L}{2}\\ \frac{\sqrt{2}}{2} & \frac{L}{2}\le\eta\le L\end{cases}$$

$$=\frac{\sqrt{3}}{18}w_{0,\,-1}(\eta)+\frac{1}{4}w_{0,\,0}(\eta)-\frac{\sqrt{3}}{18}w_{0,\,1}(\eta)+\frac{1}{2}w_{1,\,0}(\eta)$$

$$=\left[\frac{\sqrt{3}}{18},\ \frac{1}{4},\ -\frac{\sqrt{3}}{18},\ 0,\ \frac{1}{2},\ 0\right]W_6(\eta)$$

Similarly, we obtain the following:

$$\int_0^\eta w_{0,1}(\eta)d\eta=\left[-\frac{1}{4\pi},\ \frac{1}{4\pi},\ 0,\ 0,\ 0,\ 0\right]W_6(\eta)$$

$$\int_0^\eta w_{1,(-1)}(\eta)d\eta=\left[0,\ 0,\ 0,\ 0,\ -\frac{1}{4\pi},\ \frac{1}{4\pi}\right]W_6(\eta)$$

$$\int_0^\eta w_{1,0}(\eta)d\eta=\left[0,\ 0,\ 0,\ \frac{\sqrt{3}}{18},\ \frac{1}{4},\ -\frac{\sqrt{3}}{18}\right]W_6(\eta)$$

$$\int_0^{\eta} w_{1,1}(\eta)d\eta = \left[0,\ 0,\ 0,\ -\frac{1}{4\pi},\ \frac{1}{4\pi},\ 0\right]W_6(\eta)$$

Thus, we have:

$$\int_0^{\eta} W(\eta)d\eta = P_1 W(\eta) \tag{8}$$

where,

$$P_1 = L\begin{bmatrix} 0 & -1/4\pi & 1/4\pi & 0 & 0 & 0 \\ \sqrt{3}/18 & 1/4 & -\sqrt{3}/18 & 0 & 1/2 & 0 \\ -1/4\pi & 1/4\pi & 0 & 0 & 0 & 0 \\ 0 & 0 & 0 & 0 & -1/4\pi & 1/4\pi \\ 0 & 0 & 0 & \sqrt{3}/18 & 1/4 & -\sqrt{3}/18 \\ 0 & 0 & 0 & -1/4\pi & 1/4\pi & 0 \end{bmatrix}$$
$$= L\begin{bmatrix} 0 & -0.079577 & 0.079577 & 0 & 0 & 0 \\ 0.096225 & 0.25 & -0.096225 & 0 & 0.5 & 0 \\ -0.079577 & 0.079577 & 0 & 0 & 0 & 0 \\ 0 & 0 & 0 & 0 & -0.079577 & 0.079577 \\ 0 & 0 & 0 & 0.096225 & 0.25 & -0.096225 \\ 0 & 0 & 0 & -0.079577 & 0.079577 & 0 \end{bmatrix} \tag{9}$$

is the CAS wavelet integration operation matrix. In the similar manner, by integrating the CAS wavelet basis twice and thrice, we obtain the operational matrices P_2 and P_3 as follows:

$$\int_0^{\eta}\int_0^{\eta} W(\eta)d\eta = P_2 W(\eta) \quad \text{and} \quad \int_0^{\eta}\int_0^{\eta}\int_0^{\eta} W(\eta)d\eta = P_3 W(\eta) \tag{10}$$

where,

$$P_2 = L^2\begin{bmatrix} -0.013989 & -0.013561 & 0.007657 & 0 & -0.039788 & 0 \\ 0.02868 & 0.040509 & -0.019426 & 0.048112 & 0.25 & -0.048112 \\ 0.007657 & 0.026226 & -0.013989 & 0 & 0.039788 & 0 \\ 0 & 0 & 0 & -0.013989 & -0.013561 & 0.007657 \\ 0 & 0 & 0 & 0.028685 & 0.040509 & -0.019426 \\ 0 & 0 & 0 & 0.007657 & 0.026226 & -0.013989 \end{bmatrix} \tag{11}$$

and,

$$P_3 = L^3\begin{bmatrix} -0.001673 & -0.001136 & 0.000432 & -0.003828 & -0.016728 & 0.003828 \\ 0.004609 & 0.004918 & -0.002295 & 0.026371 & 0.072337 & -0.021741 \\ 0.003396 & 0.004302 & -0.002155 & 0.003828 & 0.023060 & -0.003828 \\ 0 & 0 & 0 & -0.001673 & -0.001136 & 0.000432 \\ 0 & 0 & 0 & 0.004609 & 0.004918 & -0.002295 \\ 0 & 0 & 0 & 0.003396 & 0.004302 & -0.002155 \end{bmatrix} \tag{12}$$

In the similar manner, we can derive an operational matrix of n^{th}-integration of order N for various M and k.

2.4. Convergence and error analysis

In this section, some theorems on the convergence and error analysis of CAS wavelets expansion have been presented.

Lemma 2.1. Let the CAS wavelet expansion of an arbitrary continuous function $f(\eta)$ converges uniformly, then this expansion converges to $f(\eta)$.

Proof. Let us consider the expansion of $f(\eta)$ in terms of CAS wavelet as follows:

$$\tilde{f}(\eta) = \sum_{n=0}^{\infty}\sum_{m\in\mathbb{Z}} a_{nm} w_{n,m}(\eta) \tag{13}$$

where $a_{nm} = \langle f(\eta), w_{n,m}(\eta)\rangle$. For fixed p and q, multiplying both sides of Eq. (13) by $w_{p,q}(\eta)$ and then integrating, justified by uniform convergence on $[0,L]$, we get:

$$\int_0^{L} \tilde{f}(\eta) w_{p,q}(\eta)\mathrm{d}\eta = \int_0^{L}\sum_{n=0}^{\infty}\sum_{m\in\mathbb{Z}} a_{nm} w_{n,m}(\eta) w_{p,q}(\eta)\, \mathrm{d}\eta$$

$$= \sum_{n=0}^{\infty}\sum_{m\in\mathbb{Z}} a_{nm} \int_0^{L} w_{n,m}(\eta) w_{p,q}(\eta)\, \mathrm{d}\eta = a_{pq}$$

Therefore, $<\tilde{f}(\eta), w_{n,m}(\eta)> = a_{nm}$. Consequently, $f(\eta)$ and $\tilde{f}(\eta)$ have equal CAS wavelet expansions and therefore $f(\eta)=\tilde{f}(\eta)$ for $\eta \in [0,L]$. Hence the proof is complete.

Theorem 2.2. Let $f(\eta)\in L^2(\mathbb{R})$ be a continuous function in the interval $[0,L]$ with bounded second derivative, say $|f''(\eta)|\le \zeta$, then the CAS wavelet expansion of $f(\eta)$ converges uniformly to it.

Proof. Let $f(\eta)\in L^2(\mathbb{R})$ be a continuous function in the interval $[0,L]$ with bounded second derivative, say $|f''(\eta)|\le \zeta$, then the CAS wavelet expansion of $f(\eta)$ is as follows:

$$f(\eta)=\sum_{n=0}^{\infty}\sum_{m\in\mathbb{Z}} a_{nm} w_{n,m}(\eta) \tag{14}$$

From Eq. (4), we have:

$$a_{nm} = \int_0^L f(\eta) w_{n,m}(\eta)\, d\eta = \int_{nL/2^k}^{(n+1)L/2^k} 2^{k/2} f(\eta) \mathrm{CAS}_m\left(\frac{2^k\eta}{L}-n\right) d\eta \tag{15}$$

By substituting $\frac{2^k\eta}{L}-n=t$ into Eq. (15), we get:

$$\begin{aligned}
a_{nm} &= \int_0^L \frac{2^{k/2}L}{2^k} f\left(\frac{(t+n)L}{2^k}\right)\mathrm{CAS}_m(t)\,dt \\
&= \frac{L}{2^{k/2}}\int_0^L f\left(\frac{(t+n)L}{2^k}\right)(\cos(2m\pi t)+\sin(2m\pi t))\,dt \\
&= \frac{L}{2^{k/2}} f\left(\frac{(t+n)L}{2^k}\right)\int_0^L(\cos(2m\pi t)+\sin(2m\pi t))\,dt \\
&\quad -\frac{L}{2^{k/2}}\int_0^L\left(f'\left(\frac{(t+n)L}{2^k}\right)\int_0^L(\cos(2m\pi t)+\sin(2m\pi t))\,dt\right)dt \\
&= \frac{L}{2^{k/2}} f\left(\frac{(t+n)L}{2^k}\right)\left.\frac{(\sin(2m\pi t)-\cos(2m\pi t))}{2m\pi}\right|_0^L \\
&\quad -\frac{L}{2^{k/2}(2m\pi)}\int_0^L\left(f'\left(\frac{(t+n)L}{2^k}\right)(\sin(2m\pi t)-\cos(2m\pi t))\right)dt \\
&= -\frac{L}{2^{3k/2}(m\pi)} f'\left(\frac{(t+n)L}{2^k}\right)\left.\frac{(-\cos(2m\pi t)-\sin(2m\pi t))}{2m\pi}\right|_0^L \\
&\quad +\frac{L}{2^{3k/2}(2m^2\pi^2)}\int_0^L\left(f''\left(\frac{(t+n)L}{2^k}\right)(-\cos(2m\pi t)-\sin(2m\pi t))\right)dt \\
&= 0-\frac{L}{2^{5k/2}(m^2\pi^2)}\int_0^L\left(f''\left(\frac{(t+n)L}{2^k}\right)\mathrm{CAS}_m(t)\right)dt
\end{aligned} \tag{16}$$

Therefore, we get:

$$\left|a_{nm}{}^2\right| = \left|\frac{L}{2^{5k/2}(m^2\pi^2)}\int_0^L\left(f''\left(\frac{(t+n)L}{2^k}\right)\mathrm{CAS}_m(t)\right)dt\right|^2 \le \left(\frac{L}{2^{5k/2}(m^2\pi^2)}\right)^2\int_0^L\left|f''\left(\frac{(t+n)L}{2^k}\right)\right|^2 dt\int_0^L|\mathrm{CAS}_m(t)|^2\,dt \tag{17}$$

Since CAS wavelets are orthonormal, we have $\int_0^L|\mathrm{CAS}_m(t)|^2\,dt=1$. Also, using $|f''(\eta)|\le\zeta$, we get:

$$|a_{nm}|^2 \le \left(\frac{L\zeta}{2^{5k/2}(m^2\pi^2)}\right)^2 \tag{18}$$

Also, we have $n\le 2^k$, therefore, we get:

$$|a_{nm}|^2 \le \left(\frac{L\zeta}{n^{5k/2}m^2\pi^2}\right)^2 \tag{19}$$

Hence the series $\sum_{n=0}^{\infty}\sum_{m\in\mathbb{Z}} a_{nm}$ is absolutely convergent. On the other hand, we can obtain:

$$\left|\sum_{n=0}^{\infty}\sum_{m\in\mathbb{Z}} a_{nm}w_{n,m}(\eta)\right| \le \sum_{n=0}^{\infty}\sum_{m\in\mathbb{Z}}|a_{nm}||w_{n,m}(\eta)| \le 2\sum_{n=0}^{\infty}\sum_{m\in\mathbb{Z}}|a_{nm}|<\infty$$

From Lemma 2.1, the series $\sum_{n=0}^{\infty}\sum_{m\in\mathbb{Z}} a_{nm}w_{n,m}(\eta)$ converges to $f(\eta)$.

Theorem 2.3. Let $f(\eta)\in L^2(\mathbb{R})$ be a continuous function in the interval $[0,L]$ and $|f(\eta)|\le\phi,\ \forall\eta\in[0,L]$. Let $\tilde{f}(\eta)$ be the approximate function of $f(\eta)$ by using CAS wavelets. Then the bound of the truncated error $E(\eta)$ is given as:

$$\|E(\eta)\|_2\le\left(\sum_{n=2^k}^{\infty}\sum_{m=-M}^{M}\xi_{nm}^2\right)^{\frac{1}{2}}+\left(\sum_{n=0}^{\infty}\sum_{m=M+1}^{\infty}\xi_{nm}^2\right)^{\frac{1}{2}}+\left(\sum_{n=0}^{\infty}\sum_{m=-\infty}^{-M-1}\xi_{nm}^2\right)^{\frac{1}{2}} \tag{20}$$

where $\xi_{nm}=\left(\dfrac{L\zeta}{n^{5k/2}m^2\pi^2}\right)$.

Proof. Any function $f(\eta)\in L^2(\mathbb{R})$ in the interval $[0,L]$ can be expanded in terms of CAS wavelets as follows:

$$f(\eta)=\sum_{n=0}^{\infty}\sum_{m\in\mathbb{Z}}a_{nm}w_{n,m}(\eta) \tag{21}$$

Let $\tilde{f}(\eta)$ be the truncated expansion of $f(\eta)$ by CAS wavelets given as follows:

$$\tilde{f}(\eta)=\sum_{n=0}^{2^k-1}\sum_{m=-M}^{M}a_{nm}w_{n,m}(\eta) \tag{22}$$

Then the error can be computed as:

$$\begin{aligned}E(\eta)=f(\eta)-\tilde{f}(\eta)&=\sum_{n=0}^{\infty}\sum_{m\in\mathbb{Z}}a_{nm}w_{n,m}(\eta)-\sum_{n=0}^{2^k-1}\sum_{m=-M}^{M}a_{nm}w_{n,m}(\eta)\\&=\sum_{n=2^k}^{\infty}\sum_{m=-M}^{M}a_{nm}w_{n,m}(\eta)+\sum_{n=0}^{\infty}\sum_{m=M+1}^{\infty}a_{nm}w_{n,m}(\eta)+\sum_{n=0}^{\infty}\sum_{m=-\infty}^{-M-1}a_{nm}w_{n,m}(\eta)\end{aligned}$$

then,

$$\|E(\eta)\|_2=\left\|\sum_{n=2^k}^{\infty}\sum_{m=-M}^{M}a_{nm}w_{n,m}(\eta)+\sum_{n=0}^{\infty}\sum_{m=M+1}^{\infty}a_{nm}w_{n,m}(\eta)+\sum_{n=0}^{\infty}\sum_{m=-\infty}^{-M-1}a_{nm}w_{n,m}(\eta)\right\|_2 \tag{23a}$$

$$\begin{aligned}\|E(\eta)\|_2&\le\left\|\sum_{n=2^k}^{\infty}\sum_{m=-M}^{M}a_{nm}w_{n,m}(\eta)\right\|_2+\left\|\sum_{n=0}^{\infty}\sum_{m=M+1}^{\infty}a_{nm}w_{n,m}(\eta)\right\|_2+\left\|\sum_{n=0}^{\infty}\sum_{m=-\infty}^{-M-1}a_{nm}w_{n,m}(\eta)\right\|_2\\&\le\left(\int_0^L\left|\sum_{n=2^k}^{\infty}\sum_{m=-M}^{M}a_{nm}w_{n,m}(\eta)\right|^2d\eta\right)^{\frac{1}{2}}+\left(\int_0^L\left|\sum_{n=0}^{\infty}\sum_{m=M+1}^{\infty}a_{nm}w_{n,m}(\eta)\right|^2d\eta\right)^{\frac{1}{2}}+\left(\int_0^L\left|\sum_{n=0}^{\infty}\sum_{m=-\infty}^{-M-1}a_{nm}w_{n,m}(\eta)\right|^2d\eta\right)^{\frac{1}{2}}\\&\le\left(\sum_{n=2^k}^{\infty}\sum_{m=-M}^{M}|a_{nm}|^2\int_0^L|w_{n,m}(\eta)|^2d\eta\right)^{\frac{1}{2}}+\left(\sum_{n=0}^{\infty}\sum_{m=M+1}^{\infty}|a_{nm}|^2\int_0^L|w_{n,m}(\eta)|^2d\eta\right)^{\frac{1}{2}}+\left(\sum_{n=0}^{\infty}\sum_{m=-\infty}^{-M-1}|a_{nm}|^2\int_0^L|w_{n,m}(\eta)|^2d\eta\right)^{\frac{1}{2}}\end{aligned} \tag{23b}$$

By using inequality (19), we get:

$$\|E(\eta)\|_2\le\left(\sum_{n=2^k}^{\infty}\sum_{m=-M}^{M}\left(\frac{L\zeta}{n^{5k/2}m^2\pi^2}\right)^2\int_0^L|w_{n,m}(\eta)|^2d\eta\right)^{\frac{1}{2}}+\left(\sum_{n=0}^{\infty}\sum_{m=M+1}^{\infty}\left(\frac{L\zeta}{n^{5k/2}m^2\pi^2}\right)^2\int_0^L|w_{n,m}(\eta)|^2d\eta\right)^{\frac{1}{2}}+\left(\sum_{n=0}^{\infty}\sum_{m=-\infty}^{-M-1}\left(\frac{L\zeta}{n^{5k/2}m^2\pi^2}\right)^2\int_0^L|w_{n,m}(\eta)|^2d\eta\right)^{\frac{1}{2}} \tag{24}$$

Since CAS wavelet basis are orthonormal, we have $\int_0^L|w_{n,m}(\eta)|^2d\eta=1$ and by taking $\xi_{nm}=\left(\dfrac{L\zeta}{n^{5k/2}m^2\pi^2}\right)$, the inequality (24) becomes:

$$\|E(\eta)\|_2\le\left(\sum_{n=2^k}^{\infty}\sum_{m=-M}^{M}\xi_{nm}^2\right)^{\frac{1}{2}}+\left(\sum_{n=0}^{\infty}\sum_{m=M+1}^{\infty}\xi_{nm}^2\right)^{\frac{1}{2}}+\left(\sum_{n=0}^{\infty}\sum_{m=-\infty}^{-M-1}\xi_{nm}^2\right)^{\frac{1}{2}}$$

Here, $\|E(\eta)\|_2\to0$ as $n,m\to\infty$ where $n=0,1,2,\ldots,2^k-1$ and $m\in\mathbb{Z}$. This proves the accuracy and stability of the proposed CASWBNT.

3. Mathematical Formulation of the Dusty Fluid Flow Problem

Consider an unsteady laminar boundary layer flow and heat transfer of a viscous incompressible of MHD dusty tangent hyperbolic fluid over a sheet placed along x-axis. The fluid flows due to stretching the sheet along the x-direction with the velocity $U_s(x,t)=sx/1-rt$ by exerting two equal and opposite forces. Here s is the stretching rate of the sheet, r is the unsteady factor and t is the time. The fluid flow in x-direction constrained in a region $y>0$. Non-linear thermal radiation and convective heat transfer are considered. The convective temperature at the surface T_f and heat transfer coefficient h of the convective heating process by conduction causes the temperature of the sheet. The magnetic dipole is lying on y-axis at a distance 'a' below the x-axis. The strong magnetic field is pointing in the x-direction. The surface temperature $T_s(x,t)=T_\infty+T_0sx^2/(1-rt)^{3/2}$ is assumed to be smaller than that of the curie temperature T_c i.e., $(T_s<T_c)$. The ambient temperature away from the surface is $T_\infty=T_c$ and there is no magnetization until the fluid begin to cool after entering into the thermal boundary layer near the surface. The flow configuration is shown in Fig. 1.

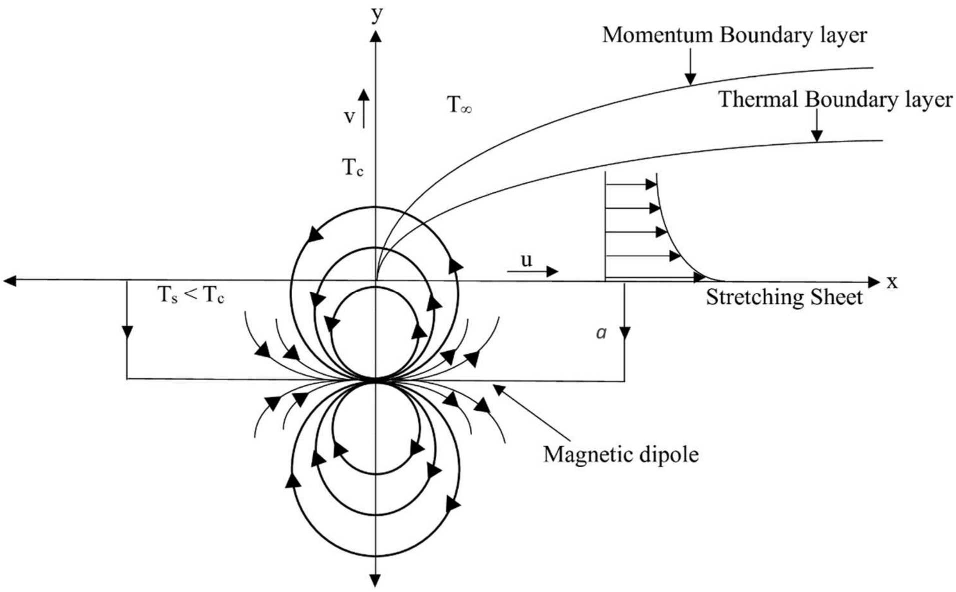

Fig. 1. Flow configuration of the problem.

The equation of tangent hyperbolic fluid is given as [8]:

$$\tau = \left[\mu_0 + (\mu_0 + \mu_\infty)\tanh(\Gamma\dot{\gamma})^{n_1}\right]\dot{\gamma} \tag{25}$$

where τ is the extra stress tensor, μ_∞ and μ_0 are the infinite and zero shear rate viscosities, respectively, n_1 power law index, Γ is time dependent material constant and $\dot{\gamma}$ is given by:

$$\dot{\gamma} = \sqrt{\frac{1}{2}\sum_i \sum_j \dot{\gamma}_{ij}\ \dot{\gamma}_{ji}} = \sqrt{\frac{1}{2}\pi}$$

Since, the case of infinite shear rate viscosity is not possible to discuss the problem, we take $\mu_\infty = 0$. The tangent hyperbolic fluid explains the shear thinning phenomena, hence $\Gamma\dot{\gamma} < 1$. Therefore, Eq. (25) becomes:

$$\begin{aligned} \tau &= \mu_0\left[(\Gamma\dot{\gamma})^{n_1}\right] \\ &= \mu_0\left[1 + n_1(\Gamma\dot{\gamma} - 1)\right]\dot{\gamma} \end{aligned} \tag{26}$$

The magnetic dipole affects the dusty tangent hyperbolic fluid flow. The magnetic scalar potential is given by [13]:

$$\Phi = \frac{\gamma^*}{2\pi}\left(\frac{x}{x^2 + (y+a)^2}\right) \tag{27}$$

where γ^* is the magnetic field strength, the magnetic field components along x and y-directions are [13]:

$$H_x = -\frac{\partial \Phi}{\partial x} = \frac{\gamma^*}{2\pi}\left(\frac{x^2 - (y+a)^2}{\left(x^2 + (y+a)^2\right)^2}\right) \tag{28}$$

$$H_y = -\frac{\partial \Phi}{\partial y} = \frac{\gamma^*}{2\pi}\left(\frac{2x(y+a)}{\left(x^2 + (y+a)^2\right)^2}\right) \tag{29}$$

The resultant magnitude of the magnetic field strength is [13]:

$$H = \left[\left(\frac{\partial \Phi}{\partial x}\right)^2 + \left(\frac{\partial \Phi}{\partial y}\right)^2\right]^{\frac{1}{2}} = \frac{\gamma^*}{2\pi}\left(\frac{1}{x^2 + (y+a)^2}\right) \tag{30}$$

$$\frac{\partial H}{\partial x} = \frac{-\gamma^*}{2\pi}\left(\frac{2x}{(y+a)^4}\right) \tag{31}$$

$$\frac{\partial H}{\partial y} = \frac{\gamma^*}{2\pi}\left(\frac{-2}{(y+a)^3} + \frac{4x^2}{(y+a)^5}\right) \tag{32}$$

The magnetization can be approximated as linear function of temperature as [13]:

$$M_0 = k_1^*(T_c - T) \tag{33}$$

where k_1^* is pyromagnetic coefficient and T_c is curie temperature.

The following assumptions are made:

- Dust particles are assumed to be spherical in shape and uniform in size.
- Dust particles number density is fixed.

Under the preceding assumptions, the governing equations for boundary layer flow and heat transfer of an unsteady dusty tangent hyperbolic fluid flow with magnetic dipole, quadratic convection, convection boundary and non-linear radiation are as follows [2-22]:

$$\frac{\partial u}{\partial x} + \frac{\partial v}{\partial y} = 0, \tag{34}$$

$$\frac{\partial u}{\partial t} + u\frac{\partial u}{\partial x} + v\frac{\partial u}{\partial y} = \upsilon(1-n_1)\frac{\partial^2 u}{\partial y^2} + \sqrt{2}\upsilon n_1\Gamma\left(\frac{\partial u}{\partial y}\right)\frac{\partial^2 u}{\partial y^2} + \frac{k_1 N_d}{\rho}\left(u_p - u\right) + g\left[\delta_1\left(T - T_\infty\right) + \delta_2\left(T - T_\infty\right)^2\right] + \frac{\mu_0 M_0}{\rho}\frac{\partial H}{\partial x} - \frac{\upsilon u}{k'}, \tag{35}$$

$$\frac{\partial u_p}{\partial x} + \frac{\partial v_p}{\partial y} = 0, \tag{36}$$

$$\frac{\partial u_p}{\partial t} + u_p\frac{\partial u_p}{\partial x} + v_p\frac{\partial u_p}{\partial y} = \frac{k_1 N_d}{\rho_p}\left(u - u_p\right), \tag{37}$$

$$\frac{\partial T}{\partial t} + u\frac{\partial T}{\partial x} + v\frac{\partial T}{\partial y} + \frac{\mu_0 T}{\rho c_p}\frac{\partial M_0}{\partial T}\left(u\frac{\partial H}{\partial x} + v\frac{\partial H}{\partial y}\right) = \frac{k_0}{\rho c_p}\left(\frac{\partial^2 T}{\partial y^2}\right) + \frac{\rho_p}{\rho\tau_T}\left(T_p - T\right) + \frac{\rho_p}{\rho c_p \tau_v}\left(u_p - u\right)^2 - \frac{1}{\rho c_p}\frac{\partial q_r}{\partial y}, \tag{38}$$

$$\rho_p c_m\left[\frac{\partial T_p}{\partial t} + u_p\frac{\partial T_p}{\partial x} + v_p\frac{\partial T_p}{\partial y}\right] = \frac{\rho_p c_p}{\tau_T}\left(T - T_p\right). \tag{39}$$

with the boundary conditions are [2-7, 23-26]:

$$\begin{gathered} u = U_s(x,t),\ \ v = 0,\ \ -k_0\frac{\partial T}{\partial y} = h(T_f - T) \ \text{ at } \ y = 0, \\ u \to 0,\ \ u_p \to 0,\ \ v_p \to v,\ \ T \to T_\infty,\ \ T_p \to T_\infty \ \ \text{ as } \ y \to \infty. \end{gathered} \tag{40}$$

Using the Rosseland approximation [45], radiative heat flux is given by:

$$q_r = -\frac{4\sigma^*}{3k^*}\frac{\partial T^4}{\partial y} \tag{41}$$

where σ^* is Steafan-Boltzmann constant and k^* is coefficient of mean absorption:

$$q_r = -\frac{16\sigma^* T^3}{3k^*}\frac{\partial T}{\partial y} \tag{42}$$

Thus, we get:

$$\frac{\partial q_r}{\partial y} = -\frac{16\sigma^*}{3k^*}\left[T^3\frac{\partial^2 T}{\partial y^2} + 3T^2\left(\frac{\partial T}{\partial y}\right)^2\right] \tag{43}$$

Substitution of Eq. (43) in Eq. (38), gives:

$$\frac{\partial T}{\partial t} + u\frac{\partial T}{\partial x} + v\frac{\partial T}{\partial y} + \frac{\mu_0 T}{\rho c_p}\frac{\partial M_0}{\partial T}\left(u\frac{\partial H}{\partial x} + v\frac{\partial H}{\partial y}\right) = \frac{k_0}{\rho c_p}\left(\frac{\partial^2 T}{\partial y^2}\right) + \frac{\rho_p}{\rho\tau_T}\left(T_p - T\right) + \frac{\rho_p}{\rho c_p\tau_v}\left(u_p - u\right)^2 + \frac{16\sigma^*}{3k^*\rho c_p}\left[T^3\frac{\partial^2 T}{\partial y^2} + 3T^2\left(\frac{\partial T}{\partial y}\right)^2\right]. \tag{44}$$

Equations (34) to (37), (39), (40) and (44) are transformed to the non-dimensional ODEs by employing the following similarity transformations [2–7]:

$$\begin{gathered} u = \frac{sx}{1-rt}f'(\eta),\ \ v = -\sqrt{\frac{s\upsilon}{1-rt}}f(\eta),\ \ u_p = \frac{sx}{1-rt}F'(\eta),\ \ v_p = -\sqrt{\frac{s\upsilon}{1-rt}}F(\eta),\ \ \eta = \sqrt{\frac{s}{\upsilon(1-rt)}}y, \\ \upsilon = \frac{\mu}{\rho},\ \ \theta(\eta) = \frac{T - T_\infty}{T_s - T_\infty} \ \text{ and } \ \theta_p(\eta) = \frac{T_p - T_\infty}{T_s - T_\infty}. \end{gathered} \tag{45}$$

Since the non-linear thermal radiation is considered, we rewrite $\theta(\eta) = \dfrac{T - T_\infty}{T_s - T_\infty}$ as:

$$T = T_\infty + (T_s - T_\infty)\theta(\eta) = T_\infty\left(1 + (T_s / T_\infty - 1)\theta(\eta)\right) \tag{46}$$

Thus, we obtain:

$$T = T_\infty\left(1 + (\theta_s - 1)\theta\right) \tag{47}$$

where $\theta_s = (T_s / T_\infty)(> 1)$ is temperature ratio parameter. Substituting Eqs. (45) and (47) into the Eqs. (34) to (37), (39), (40) and (44), we get:

$$f'''(\eta)(1 - n_1 + n_1 We\, f''(\eta)) + f(\eta)f''(\eta) - (f'(\eta))^2 - A_S\left(f'(\eta) + (\eta/2)f''(\eta)\right) + \omega\left(\theta(\eta) + \delta^*(\theta(\eta))^2\right) + l\beta_v\left(F'(\eta) - f'(\eta)\right) - Pf'(\eta) - \frac{2\beta^*\theta(\eta)}{(\eta+\alpha)^4} = 0 \tag{48}$$

$$A_S\left(F'(\eta) + (\eta/2)F''(\eta)\right) - F(\eta)F''(\eta) + (F'(\eta))^2 + \beta_v\left(F'(\eta) - f'(\eta)\right) = 0 \tag{49}$$

$$\begin{aligned}&\theta''(\eta) + \Pr\left(f(\eta)\theta'(\eta) - 2f'(\eta)\theta(\eta) - A_S\left(3\theta(\eta) + \eta\theta'(\eta)\right)/2\right) + \Pr l\beta_t\left(\theta_p(\eta) - \theta(\eta)\right) + \Pr l\beta_v Ec\left(F'(\eta) - f'(\eta)\right)^2 + \left(\theta(\eta) - \varepsilon^*\right)\frac{2\beta^*\lambda f(\eta)}{(\eta+\alpha)^3} \\ &+ R\left(\left(1 + (\theta_s - 1)\theta(\eta)\right)^3\theta''(\eta) + 3\left(\left(1 + (\theta_s - 1)\theta(\eta)\right)^2(\theta_s - 1)\left(\theta'(\eta)\right)^2\right) - \beta^*\lambda \mathrm{Re}_x\left(\theta(\eta) - \varepsilon^*\right)\left(\frac{2f'(\eta)}{(\eta+\alpha)^4} + \frac{4f(\eta)}{(\eta+\alpha)^5}\right)\right) = 0\end{aligned} \tag{50}$$

$$F(\eta)\theta_p'(\eta) - 2F'(\eta)\theta_p(\eta) - A_S\left(3\theta_p(\eta) + \eta\theta_p'(\eta)\right)/2 - \beta_t\gamma_1\left(\theta_p(\eta) - \theta(\eta)\right) = 0 \tag{51}$$

with the boundary conditions:

$$\begin{aligned} &f(\eta) = 0, \quad f'(\eta) = 1, \quad \theta'(\eta) = -Bi\left(1 - \theta(\eta)\right) \quad \text{at } \eta = 0, \\ &f'(\eta) \to 0, \quad F'(\eta) \to 0, \quad F(\eta) \to f(\eta), \quad \theta(\eta) \to 0, \quad \theta_p(\eta) \to 0, \quad \text{as } \eta \to \infty \end{aligned} \tag{52}$$

where $We = \Gamma\sqrt{2s^3x^2 / \upsilon(1-rt)^3}$ is the Weissenberg number, $A_S = r/s$ and $P = \upsilon(1-rt)/sk'$ are unsteady and porosity parameters, respectively, $\omega = Gr/\mathrm{Re}_x^2 = g\delta_1(T_s - T_\infty)x/U_s^2$ mixed convection parameter, $Gr = g\delta_1(T_s - T_\infty)x^3/\upsilon^2$ is the Grashoff number, $\mathrm{Re}_x = U_s x/\upsilon$ local Reynolds number, $\delta^* = \delta_2(T_s - T_\infty)/\delta_1$ is quadratic convection parameter, $\beta_v = (1-rt)/\tau_v s$ and $\beta_t = (1-rt)/\tau_T s$ are fluid-particle interaction parameter for velocity and heat transfer, respectively, $\lambda = \mu^2 s/\left(k_0\rho(T_c - T_s)(1-rt)\right)$ viscous dissipation parameter, $\varepsilon^* = T_c/(T_c - T_s)$ curie temperature ratio, ρ and $\rho_p = m_1 N_d$ are the density of fluid and dust particles phase, respectively, $\tau_v = m_1/k_1$ is dust particles relaxation time, $l = m_1 N_d/\rho = \rho_p/\rho$ dust particles mass concentration, $\alpha = \sqrt{s/(\upsilon(1-rt))}a$ dimensionless distance, τ_T is thermal equilibrium time, $\beta^* = \mu_0 k_1^*(T_c - T_s)\rho\gamma^*/2\pi\mu^2$ ferro-hydrodynamic interaction parameter, $\gamma_1 = c_p/c_m$ the specific heat ratio, $\Pr = \mu c_p/k_0$ Prandtl number, $Bi = \left(h\sqrt{\upsilon(1-rt)/s}\right)/k_0$ is the Biot number, $R = 16\sigma^* T_\infty^3/(3k^*k_0)$ radiation parameter and $Ec = U_s^2/\left(c_p(T_s - T_\infty)\right)$ Eckert number.

3.1. Skin friction coefficient and local Nusselt number

The physical quantities of relevance from an engineering perspective, skin-friction coefficient and local Nusselt number are given by [2, 7–12]:

$$C_f = \frac{\tau_s}{\rho_f U_s^2} \quad \text{and} \quad Nu_x = \frac{x(q_s + q_r)}{k_0(T_s - T_\infty)} \tag{53}$$

Here τ_s is the skin friction and q_s is the heat flux at the surface which are given by [2, 7–12]:

$$\tau_s = \mu\left((1-n_1)\left(\frac{\partial u}{\partial y}\right) + \frac{n_1\Gamma}{\sqrt{2}}\left(\frac{\partial u}{\partial y}\right)^2\right)_{y=0} \quad \text{and} \quad q_s = -k_0\left(\frac{\partial T}{\partial y}\right)_{y=0} \tag{54}$$

Utilisation of dimensionless variables from Eqs. (45) gives:

$$C_f\sqrt{\mathrm{Re}_x} = (1-n_1)f''(0) + \frac{n_1}{2}We\left(f''(0)\right)^2 \quad \text{and} \quad Nu_x/\sqrt{\mathrm{Re}_x} = -\theta'(0)\left(1 + R\left(1 + (\theta_s - 1)\theta(0)\right)^3\right) \tag{55}$$

3.2. Entropy analysis

Entropy analysis is prominent in heat transfer problems. It is essential to study thermal energy irreversibility in the system. The entropy generation rate for tangent hyperbolic fluid due to magnetic field, heat transfer and fluid friction is given as follows [30]:

$$\acute{S}_{gen} = \frac{k_0}{T_\infty^2}\left(1 + \frac{16\sigma T^3}{3k^*k_0}\right)\left(\frac{\partial T}{\partial y}\right)^2 + \frac{\mu}{T_\infty}\left((1-n_1) + \frac{n_1\Gamma}{\sqrt{2}}\left(\frac{\partial u}{\partial y}\right)\right)\left(\frac{\partial u}{\partial y}\right)^2 \tag{56}$$

The non-dimensional form of entropy generation E_{gen} is obtained by the ratio of $\acute{S}_{gen}$ to the entropy generation characteristic $\acute{S}_0$, which is defined as:

$$\acute{S}_0 = k_0(T_s - T_\infty)^2/\left(x^2T_\infty^2\right)$$

Thus, the non-dimensional form of entropy generation E_{gen} is:

$$E_{gen}=\frac{\acute{S}_{gen}}{\acute{S}_0}=\frac{\left(\frac{k_0}{T_\infty^2}\left(1+\frac{16\sigma T^3}{3k^*k_0}\right)\left(\frac{\partial T}{\partial y}\right)^2+\frac{\mu}{T_\infty}\left((1-n_1)+\frac{n_1\Gamma}{\sqrt{2}}\left(\frac{\partial u}{\partial y}\right)\right)\left(\frac{\partial u}{\partial y}\right)^2\right)}{k_0(T_s-T_\infty)^2/\left(x^2T_\infty^2\right)} \tag{57}$$

Utilising the similarity transformation Eqs. (45) we obtain:

$$E_{gen}=\mathrm{Re}_x\left(1+R(1+(\theta_s-1)\theta)^3\right)\theta'^2+\left(Br\,\mathrm{Re}_x/t_d\right)\left[(1-n_1)+(n_1/2)We\,f''\right](f'')^2 \tag{58}$$

where $Br=\mu U_s^2/\left(k_0(T_s-T_\infty)\right)$ is the Brinkman number and $t_d=(T_s-T_\infty)/T_\infty$ is the temperature difference variable. The Bejan number (Be) is defined as the proportion of entropy production as a result of heat transmission to the entire entropy generation:

$$Be=\frac{\mathrm{Re}_x\left(1+R(1+(\theta_s-1)\theta)^3\right)\theta'^2}{\mathrm{Re}_x\left(1+R(1+(\theta_s-1)\theta)^3\right)\theta'^2+\left(Br\,\mathrm{Re}_x/t_d\right)\left[(1-n_1)+(n_1/2)We\,f''\right](f'')^2} \tag{59}$$

4. CAS Wavelet Based Numerical Technique of Solution

Consider the system of third order non-linear ODEs:

$$\begin{aligned} Y_1'''(\eta) &= f_1(\eta,Y_1,Y_2,Y_1',Y_2',Y_1'',Y_2''),\\ Y_2'''(\eta) &= f_2(\eta,Y_1,Y_2,Y_1',Y_2',Y_1'',Y_2''), \quad 0\le\eta\le L, \end{aligned} \tag{60}$$

subject to the boundary conditions below:

$$\begin{aligned} Y_1(0) &= \lambda_1,\ Y_1'(0)=\lambda_2,\ Y_1'(L)=\lambda_3\\ Y_2(0) &= \lambda_4,\ Y_2'(0)=\lambda_5,\ Y_2'(L)=\lambda_6 \end{aligned} \tag{61}$$

where $\lambda_1,\lambda_2,\lambda_3,\lambda_4,\lambda_5$ and λ_6 are real constants. We approximate the highest order derivative in first equation of the system of Eqs. (60) in terms of CAS wavelets as follows:

$$Y_1'''(\eta)=A^TW(\eta) \tag{62}$$

where $A^T=[a_{0(-M)},a_{0(-M+1)},\dots,a_{0M},a_{1(-M)},\dots,a_{1M},\dots,a_{(2^k-1)(-M)},\dots,a_{(2^k-1)M}]$ is the unknown CAS wavelet coefficient matrix and $W(\eta)$ CAS wavelet basis matrix. Integration of Eq. (62) from 0 to η gives:

$$Y_1''(\eta)=Y_1''(0)+A^TP_1W(\eta) \tag{63}$$

Integration of Eq. (63) from 0 to η gives:

$$Y_1'(\eta)=Y_1'(0)+\eta Y_1''(0)+A^TP_2W(\eta) \tag{64}$$

Using boundary condition Eqs. (61) in Eq. (64), we get:

$$Y_1'(\eta)=\lambda_2+\eta Y_1''(0)+A^TP_2W(\eta) \tag{65}$$

Substituting $\eta=L$ in Eq. (65) and applying boundary condition Eqs. (61), we get:

$$Y_1''(0)=\left(\lambda_3-\lambda_2-A^TP_2W(L)\right)/L \tag{66}$$

Substitution of Eq. (66) in Eqs. (63) and (65) gives:

$$Y_1''(\eta)=\left(\lambda_3-\lambda_2-A^TP_2W(L)\right)/L+A^TP_1W(\eta) \tag{67}$$

$$Y_1'(\eta)=\lambda_2+\eta\left(\lambda_3-\lambda_2-A^TP_2W(L)\right)/L+A^TP_2W(\eta) \tag{68}$$

Integration of Eq. (68) from 0 to η gives:

$$Y_1(\eta)=Y_1(0)+\eta\lambda_2+\eta^2\left(\lambda_3-\lambda_2-A^TP_2W(L)\right)/(2L)+A^TP_3W(\eta) \tag{69}$$

Using boundary condition Eqs. (61) in Eq. (69), we get:

$$Y_1(\eta)=\lambda_1+\eta\lambda_2+\eta^2\left(\lambda_3-\lambda_2-A^TP_2W(L)\right)/(2L)+A^TP_3W(\eta) \tag{70}$$

Similarly, we approximate the second equation of system of Eqs. (60) and obtain the following expressions:

$$Y_2'''(\eta)=B^TW(\eta) \tag{71}$$

Integration of Eq. (71) from 0 to η gives:

$$Y_2''(\eta) = Y_2''(0) + B^T P_1 W(\eta) \tag{72}$$

Integration of Eq. (72) from 0 to η and using boundary condition Eqs. (61) gives:

$$Y_2'(\eta) = \lambda_5 + \eta Y_2''(0) + B^T P_2 W(\eta) \tag{73}$$

Substituting $\eta = L$ in Eq. (73) and applying boundary condition Eqs. (61) we get:

$$Y_2''(0) = \left(\lambda_6 - \lambda_5 - B^T P_2 W(L)\right) / L \tag{74}$$

Substitution of Eq. (74) in Eqs. (72) and (73) gives:

$$Y_2''(\eta) = \left(\lambda_6 - \lambda_5 - B^T P_2 W(L)\right) / L + B^T P_1 W(\eta) \tag{75}$$

$$Y_2'(\eta) = \lambda_5 + \eta\left(\lambda_6 - \lambda_5 - B^T P_2 W(L)\right) / L + B^T P_2 W(\eta) \tag{76}$$

Integration of Eq. (76) from 0 to η and using boundary condition Eqs. (61) gives:

$$Y_2(\eta) = \lambda_4 + \eta\lambda_5 + \eta^2\left(\lambda_6 - \lambda_5 - B^T P_2 W(L)\right) / (2L) + B^T P_3 W(\eta) \tag{77}$$

Substituting Eqs. (62), (67), (68), (70), (71), (75) – (77) in the given system (60) and discretizing to N collocation points $\eta_l = (l - 0.5)L / N$, $l = 1,2,.......,N$ gives the set of $2N$ algebraic equations. Solving this system using Newton's method [46], we get the unknown CAS wavelet coefficients matrices A^T and B^T and by substituting these coefficients in Eqs. (70) and (77) we get the solutions of given system of differential Eqs. (60). The same procedure is continued for the system containing more than two differential equations of any order n.

5. Implementation of CAS Wavelet Based Numerical Technique

In this section, the CASWBNT is implemented on the test problem with the exact solutions to validate the method. This test problem is considered because the exact solutions of this problem is available and the considered dusty fluid problem is handled in a similar way to the test problem. This allows us to compare the results obtained by the proposed method with the exact solutions and the solutions obtained by the Runge-Kutta Fehlberg 4^{th} – 5^{th} order (RKF45) method. The accuracy of the CASWBNT is assessed in terms of the following error norms:

$$\text{Absolute error} = |y_l - \tilde{y}_l|,\ l = 1,2,.......,N \tag{78}$$

$$\text{Relative error} = |y_l - \tilde{y}_l| / |y_l|,\ l = 1,2,.......,N \tag{79}$$

$$\text{Maximum absolute error} = L_\infty \text{ error norm} = L_\infty = Max|y_l - \tilde{y}_l| \tag{80}$$

$$L_2 \text{ error norm} = L_2 = \left[\sum_{l=1}^{N} |y_l - \tilde{y}_l|^2\right]^{1/2} \tag{81}$$

$$\text{Maximum Relative Error} = L_{MRE} = Max\left(|y_l - \tilde{y}_l| / |y_l|\right) \tag{82}$$

$$\text{Relative Power Deviations (\%)} = L_{RPD} = \sum_{l=1}^{N}\left(|y_l - \tilde{y}_l|^2 / |y_l|^2\right) \times 100 \tag{83}$$

$$\text{Root Mean Square Error} = L_{RMSE} = \sqrt{\frac{1}{N}\sum_{l=1}^{N}(y_l - \tilde{y}_l)^2} \tag{84}$$

where y_l and $\tilde{y}_l$ are the exact and approximate solution respectively at the l^{th} point. The considered dusty tangent hyperbolic fluid problem is solved using CASWBNT in this section.

Test Problem 5.1. Consider the system of ODEs [47]:

$$Y_1''(\eta) + \eta Y_1(\eta) + \eta Y_2(\eta) = 2 \tag{85}$$

$$Y_2''(\eta) + 2\eta Y_2(\eta) + 2\eta Y_1(\eta) = -2, \qquad \eta \in [0,1] \tag{86}$$

with boundary conditions:

$$\begin{gathered} Y_1(0) = 0,\ \ Y_1(1) = 0 \\ Y_2(0) = 0,\ \ Y_2(1) = 0 \end{gathered} \tag{87}$$

The given system of equations (85) and (86) is solved using CASWBNT as follows:
First, we approximate highest order derivative of Eq. (85) in terms of CAS wavelets as:

$$Y_1''(\eta) = A^T W(\eta) \tag{88}$$

Integration of Eq. (88) from 0 to η gives:

$$Y_1'(\eta) = Y_1'(0) + A^T P_1 W(\eta) \tag{89}$$

Integration of Eq. (89) from 0 to η and using boundary condition Eqs. (87) gives:

$$Y_1(\eta) = \eta Y_1'(0) + A^T P_2 W(\eta) \tag{90}$$

Substituting $\eta = 1$ in Eq. (90) and applying boundary condition Eqs. (87), we get:

$$Y_1'(0) = -A^T P_2 W(1) \tag{91}$$

Substitution of Eq. (91) in Eqs. (89) and (90) gives:

$$Y_1'(\eta) = A^T P_1 W(\eta) - A^T P_2 W(1) \tag{92}$$

$$\text{and} \quad Y_1(\eta) = A^T P_2 W(\eta) - \eta A^T P_2 W(1) \tag{93}$$

Similarly, we approximate highest order derivative of Eq. (86) in terms of CAS wavelets as:

$$Y_2''(\eta) = B^T W(\eta) \tag{94}$$

Integration of Eq. (94) from 0 to η gives:

$$Y_2'(\eta) = Y_2'(0) + B^T P_1 W(\eta) \tag{95}$$

Integration of Eq. (95) from 0 to η and using boundary condition Eqs. (87) gives:

$$Y_2(\eta) = \eta Y_2'(0) + B^T P_2 W(\eta) \tag{96}$$

Substituting $\eta = 1$ in Eq. (96) and applying boundary condition Eqs. (87), we get:

$$Y_2'(0) = -B^T P_2 W(1) \tag{97}$$

Substitution of Eq. (97) in Eqs. (95) and (96) gives:

$$Y_2'(\eta) = B^T P_1 W(\eta) - B^T P_2 W(1) \tag{98}$$

$$\text{and} \quad Y_2(\eta) = B^T P_2 W(\eta) - \eta B^T P_2 W(1) \tag{99}$$

Substituting Eqs. (88), (92) to (94), (98), (99) in the given system (85) and (86), we get:

$$A^T W(\eta) + \eta\left(A^T P_2 W(\eta) - \eta A^T P_2 W(1)\right) + \eta\left(B^T P_2 W(\eta) - \eta B^T P_2 W(1)\right) = 2 \tag{100}$$

$$B^T W(\eta) + 2\eta\left(B^T P_2 W(\eta) - \eta B^T P_2 W(1)\right) + 2\eta\left(A^T P_2 W(\eta) - \eta A^T P_2 W(1)\right) = -2 \tag{101}$$

Discretizing the system of Eqs. (100) and (101) to N collocation points $\eta_l = (l - 0.5)L/N$, $l = 1,2,\ldots\ldots,N$ gives the set of $2N$ algebraic equations. For instance, for $N = 6$ and $L = 1$ the 6 collocation points are given by $\eta_1 = 1/12$, $\eta_2 = 3/12$, $\eta_3 = 5/12$, $\eta_4 = 7/12$, $\eta_5 = 9/12$ and $\eta_6 = 11/12$. Now discretizing both the Eqs. (100) and (101) to each of these 6 collocation points we obtain the system of 12 algebraic equations.

Solving this set of $2N$ algebraic equations using Newton's method [46], we get the unknown coefficient matrices A^T and B^T and by substituting these matrices in Eqs. (93) and (99), we get the solutions of given system of differential Eqs. (85) and (86). The results acquired are compared with the shooting technique based RKF45 and exact solutions $Y_1(\eta) = \eta^2 - \eta$ and $Y_2(\eta) = \eta - \eta^2$ [47] at different points $\eta \in [0,1]$ as shown in Tables 1 and 2 for $N = 6$ (M = 1 and k = 1) and in Figs. 2 and 3 for $N = 20$ (M = 2 and k = 2). The error analysis for the solutions $Y_1(\eta)$ and $Y_2(\eta)$ for diverse N are given in Tables 3 and 4, respectively.

Dusty Fluid Problem 5.2. The governing Eqs. (48) to (51) of the considered dusty tangent hyperbolic fluid problem constitutes the non-linear system of ODEs. We use CASWBNT to solve this system as follows:

To apply CASWBNT, it is necessary to choose the finite value $\eta_\infty = L$ for $\eta \to \infty$. We choose $\eta_\infty = L = 5$ and consider the interval $\eta \in [0,5]$ in our analysis.

First, we assume the highest order derivative in Eq. (48) of the system as follows:

$$f'''(\eta) = A^T W(\eta) \tag{102}$$

Table 1. CASWBNT results for $Y_1(\eta)$ of test problem 5.1 are compared with RKF45 and exact solution for N = 6.

η (= 1 / 6)	CASWBNT Solution	RKF45 Solution	Exact Solution	CASWBNT Absolute Error	RKF45 Absolute Error
0	0.000000000	0.000000000	0.000000000	0	0
1	-0.138888889	-0.138888889	-0.138888889	1.603E-11	1E-10
2	-0.222222222	-0.222222222	-0.222222222	2.009E-11	1E-10
3	-0.250000000	-0.250000000	-0.250000000	3.363E-12	2E-10
4	-0.222222222	-0.222222222	-0.222222222	3.484E-11	2E-10
5	-0.138888889	-0.138888889	-0.138888889	2.994E-12	3E-10
6	0.000000000	0.000000000	0.000000000	0	3E-10

Table 2. CASWBNT results for $Y_2(\eta)$ of test problem 5.1 are compared with RKF45 and exact solution for N = 6.

η (= 1 / 6)	CASWBNT Solution	RKF45 Solution	Exact Solution	CASWBNT Absolute Error	RKF45 Absolute Error
0	0.000000000	0.000000000	0.000000000	0	0
1	0.138888889	0.138888889	0.138888889	2.836E-12	1E-10
2	0.222222222	0.222222222	0.222222222	4.783E-11	1E-10
3	0.250000000	0.250000000	0.250000000	2.413E-11	2E-10
4	0.222222222	0.222222222	0.222222222	3.272E-11	2E-10
5	0.138888889	0.138888889	0.138888889	1.251E-11	3E-10
6	0.000000000	-0.000000000	0.000000000	0	3E-10

Table 3. Error analysis of CASWBNT and RKF45 for $Y_1(\eta)$ of test problem 5.1 for diverse N.

N	CASWBNT					RKF45				
	L_∞	L_2	L_{MRE}	L_{RPD}	L_{RMSE}	L_∞	L_2	L_{MRE}	L_{RPD}	L_{RMSE}
6	3.484E-11	4.353-11	1.567E-10	4.674E-18	1.777E-11	3E-10	5.291E-10	2.160E-9	6.836E-16	2.160E-10
10	9.996E-12	1.671E-11	3.998E-11	5.876E-19	5.286E-12	4E-11	4.898E-11	2.222E-10	9.876E-18	1.549E-11
12	4.105E-11	7.328E-11	1.847E-10	1.138E-17	2.115E-11	2.4E-10	5.390E-10	3.010E-9	1.411E-15	1.556E-10
20	3.777E-12	1.278E-11	5.296E-11	1.283E-18	2.859E-12	2E-11	3.162E-11	4.210E-10	2.019E-17	7.071E-12
28	4.765E-11	1.240E-10	2.351E-10	4.215E-17	2.267E-11	4E-10	9.660E-10	1.103E-8	1.796E-14	1.825E10
36	5.717E-11	1.689E-10	3.313E-10	7.434E-17	2.816E-11	5.9E-10	1.781E-9	2.036E-8	6.272E-14	2.969E-10

Table 4. Error analysis of CASWBNT and RKF45 for $Y_2(\eta)$ of test problem 5.1 for diverse N.

N	CASWBNT					RKF45				
	L_∞	L_2	L_{MRE}	L_{RPD}	L_{RMSE}	L_∞	L_2	L_{MRE}	L_{RPD}	L_{RMSE}
6	4.783E-11	6.408E-11	2.152E-10	8.588E-18	2.616E-11	3E-10	5.291E-10	2.160E-9	6.836E-16	2.160E-10
10	1.246E-11	2.562E-11	8.096E-11	2.552E-18	8.103E-12	4E-11	4.898E-11	2.222E-10	9.876E-18	1.549E-11
12	4.926E-11	7.628E-11	2.026E-10	1.178E-17	2.202E-11	2.4E-10	5.390E-10	3.010E-9	1.411E-15	1.556E-10
20	5.438E-14	1.123E-13	6.555E-13	1.094E-22	2.513E-14	2E-11	3.162E-11	4.210E-10	2.019E-17	7.071E-12
28	4.895E-11	1.199E-10	2.907E-10	4.076E-17	2.267E-11	4E-10	9.660E-10	1.103E-8	1.796E-14	1.825E10
36	5.711E-11	1.755E-10	2.847E-10	7.926E-17	2.926E-11	5.9E-10	1.781E-9	2.036E-8	6.272E-14	2.969E-10

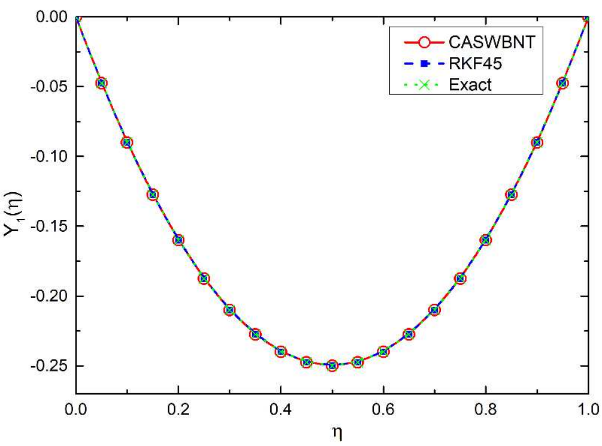

Fig. 1. CASWBNT results for $Y_1(\eta)$ of test problem 5.1 are compared with RKF45 and exact solution for N = 20.

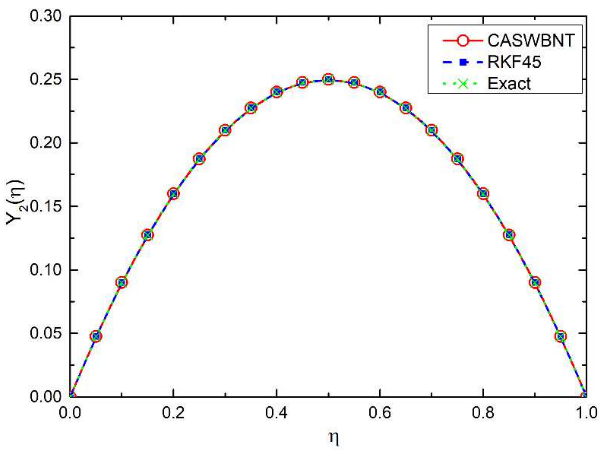

Fig. 2. CASWBNT results for $Y_2(\eta)$ of test problem 5.1 are compared with RKF45 and exact solution for N = 20.

Integration of Eq. (102) from 0 to η gives:

$$f''(\eta) = f''(0) + A^T P_1 W(\eta) \tag{103}$$

Integration of Eq. (103) from 0 to η and applying the boundary condition (52) gives:

$$f'(\eta) = 1 + \eta f''(0) + A^T P_2 W(\eta) \tag{104}$$

Substituting $\eta = L$ in Eq. (104) and applying boundary condition (52), we get:

$$f''(0) = -\left(1 + A^T P_2 W(L)\right) / L \tag{105}$$

Substituting Eq. (105) in Eqs. (103) and (104), we get:

$$f''(\eta) = A^T P_1 W(\eta) - \left(1 + A^T P_2 W(L)\right) / L \tag{106}$$

$$f'(\eta) = 1 - \frac{\eta}{L}\left(1 + A^T P_2 W(L)\right) + A^T P_2 W(\eta) \tag{107}$$

Integrating Eq. (107) from 0 to η and applying boundary condition (52), we get:

$$f(\eta) = \eta - \eta^2 \left(1 + A^T P_2 W(L)\right) / (2L) + A^T P_3 W(\eta) \tag{108}$$

In similar manner, we approximate highest order derivative of Eqs. (49) to (51) in terms of CAS wavelets and obtain the following expressions:

$$F''(\eta) = B^T W(\eta)\,,\ \theta''(\eta) = C^T W(\eta) \ \text{ and } \ \theta_p'(\eta) = D^T W(\eta) \tag{109}$$

Integrating Eq. (107) from 0 to η, we get:

$$F'(\eta) = F'(0) + B^T P_1 W(\eta) \tag{110}$$

$$\theta'(\eta) = \theta'(0) + C^T P_1 W(\eta) \tag{111}$$

$$\theta_p(\eta) = \theta_p(0) + D^T P_1 W(\eta) \tag{112}$$

Substituting $\eta = L$ in Eqs. (110) and (112) and applying the boundary condition (52) and simplifying, we get:

$$F'(0) = -B^T P_1 W(L) \tag{113}$$

$$\theta_p(0) = -D^T P_1 W(L) \tag{114}$$

Substituting Eqs. (113) and (114) into Eqs. (110) and (112), respectively, we get:

$$F'(\eta) = B^T P_1 W(\eta) - B^T P_1 W(L) \tag{115}$$

$$\theta_p(\eta) = D^T P_1 W(\eta) - D^T P_1 W(L) \tag{116}$$

By applying boundary condition (52) to Eq. (111) and simplifying, we get:

$$\theta'(\eta) = -Bi\left(1 - \theta(0)\right) + C^T P_1 W(\eta) \tag{117}$$

Integrating Eqs. (115) and (117) from 0 to η, we get:

$$F(\eta) = F(0) + B^T P_2 W(\eta) - \eta B^T P_1 W(L) \tag{118}$$

$$\begin{aligned} \theta(\eta) &= \theta(0) - \eta Bi\left(1 - \theta(0)\right) + C^T P_2 W(\eta) \\ &= (1 + \eta Bi)\theta(0) - \eta Bi + C^T P_2 W(\eta) \end{aligned} \tag{119}$$

Substituting $\eta = L$ in Eqs. (118) and (119) and applying boundary condition (52), we get:

$$F(0) = L - L\left(1 + A^T P_2 W(L)\right) / 2 + A^T P_3 W(L) - B^T P_2 W(L) + LB^T P_1 W(L) \tag{120}$$

$$\theta(0) = \left(LBi - C^T P_2 W(L)\right) / (1 + LBi) \tag{121}$$

Substituting Eqs. (120) and (121) into Eqs. (118), (117) and (119) and simplifying, we get:

$$F(\eta) = B^T P_2 W(\eta) + L - \frac{L}{2}\left(1 + A^T P_2 W(L)\right) + A^T P_3 W(L) - B^T P_2 W(L) + (L-\eta) B^T P_1 W(L) \tag{122}$$

$$\theta'(\eta) = -Bi\left(\frac{1 + C^T P_2 W(L)}{(1+LBi)}\right) + C^T P_1 W(\eta) \tag{123}$$

$$\theta(\eta) = \frac{(1+\eta Bi)}{(1+LBi)}\left(LBi - C^T P_2 W(L)\right) - \eta Bi + C^T P_2 W(\eta) \tag{124}$$

Substituting Eqs. (102), (106) - (109), (115), (116), (122) – (124) in the governing Eqs. (48) to (51) and discretizing to N collocation points $\eta_l = (l-0.5)L/N,\ l = 1,2,......,N,$ we get the set of $4N$ algebraic equations. Solving this system using Newton's method [46], we obtain the unknown CAS coefficients matrices A^T, B^T, C^T and D^T. By substituting these coefficients in in Eqs. (108), (122), (124) and (116), we obtain the numerical solutions $f(\eta)$, $F(\eta)$, $\theta(\eta)$ and $\theta_P(\eta)$ of the governing differential equations (48) to (51).

6. Results and Discussion

The CAS wavelet based numerical technique (CASWBNT) is developed for the solution of the set of non-linear ODEs arising in the study of an unsteady dusty tangent hyperbolic fluid flow over a stretching sheet through porous medium with magnetic dipole effect, quadratic convection, convection boundary, non-linear radiation and entropy generation. The convergence and error analysis validate the method. To check the validity and accuracy, the proposed technique is implemented on the test problem having the exact solution. The results acquired by CASWBNT are compared with the shooting technique based RKF45 method and the exact solutions as demonstrated in Tables 1 and 2 for $N = 6$ $(M = 1$ and $k = 1)$ and in Figs. 2 and 3 for $N = 20$ $(M = 2$ and $k = 2)$. It is observed that the solutions obtained by CASWBNT are very near to the exact solutions in contrast to the RKF45 method. Tables 3 and 4 demonstrate the error analysis using different error norms for the results $Y_1(\eta)$ and $Y_2(\eta)$ of the test problem 5.1 obtained by CASWBNT and RKF45 method for various N, respectively. It is observed that the CASWBNT solutions are highly accurate even for small number of collocation points N and accuracy increases as N increases.

The considered dusty tangent hyperbolic fluid problem is solved using CASWBNT. For fixed parameters $Bi \to \infty$, $A_s = Ec = Pr = Re_x = P = R = \gamma_1 = l = \alpha = 0,\ \theta_s = \lambda = \varepsilon^* = \beta_v = \beta_t = \omega = \beta^* = 0$ and $\delta^* = 0$, the present model gets reduced to the model for which the skin friction coefficient $C_f\sqrt{Re_x}$ values are given in the literature [8–11] so that, the CASWBNT is validated by comparing the skin friction coefficient values obtained by CASWBNT with those given in the literature [8–11]. This comparison is shown in Table 5. Clearly, the CASWBNT solutions resembles the results given in the literature [8–11]. Similarly, the values of $-\theta'(0)$ determined by CASWBNT are compared with those found in the published works [6, 7, 14] for different Pr values for $Bi \to \infty$, $A_s = Ec = n_1 = We = P = R = \gamma_1 = l = \theta_s = \omega = 0,\ \beta^* = \beta_v = \beta_t = \alpha = \lambda = \varepsilon^* = Re_x = 0$ and $\delta^* = 0$ in Table 6. It is observed that the values obtained by CASWBNT coincides with the previously published results [6, 7, 14]. These comparisons validate the proposed technique. Thus, the CASWBNT is reliable, fast computational, simple and efficient tool to solve the system of ODEs.

The considered dusty tangent hyperbolic fluid problem is solved using CASWBNT. The impact of diverse physical quantities on velocity and temperature profile of dusty tangent hyperbolic fluid are studied graphically as shown in Figs. 4 to 24. We have used the values $A_S = 0.3$, $Ec = 1$, $Pr = 3$, $P = 0.4$, $R = 1$, $Bi = 3$, $\gamma_1 = 1.8$, $l = 0.5$, $n_1 = 0.3$, $\theta_s = 1.2$, $\beta_v = 0.5$, $\omega = 2$, $\beta_t = 0.5$, $We = 0.4$, $Re_x = 1$, $\alpha = 0.7$, $\lambda = 0.8$, $\varepsilon^* = 1$, $\delta^* = 0.8$, $\beta^* = 0.4$, $Br = 1$ and $t_d = 0.5$ throughout our analysis.

Figures 4 and 5 describe the impact of power law index parameter n_1 on velocity and thermal attribute. For acceleration in n_1, the velocity declines and temperature increases. As the power law index improves, the fluid nature changes from shear thinning to shear thickening. This implies the improvement in the viscosity. Increase in viscosity slow down the fluid motion. Hence the velocity declines. Increase in viscosity improves the friction between the fluid layers which generates the heat and hence temperature augments as n_1 elevates. Also, a very small improvement in temperature is observed for increasing n_1. Figures 6 and 7 demonstrate the velocity and thermal variation for diverse Weissenberg number We, respectively. With the enhancement of We, the velocity declines and temperature uplifts. We is the association of relaxation time of the fluid and a certain process time. In simple steady shear, the Weissenberg number is defined as the shear rate times the relaxation time. It increases the thickness of the fluid. For higher We, the relaxation time improves and hence more resistance is offered to the flow. Therefore, We improves the fluid thickness. The improvement in fluid thickness slows down the fluid motion. Thus, as We accelerates, the fluid velocity depreciates. The increase in fluid thickness enhances the friction between the fluid layers which produces heat and hence the temperature of the fluid escalates. Also, a very small increase in temperature is noticed as We improves.

Table 5. Comparison of CASWBNT values of $C_f\sqrt{Re_x}$ with the values given in the literature [8-11] for $Bi \to \infty$, $A_s = Ec = Pr = Re_x = P = 0$, $R = \gamma_1 = l = \theta_s = \alpha = \lambda = 0,\ \varepsilon^* = \beta_v = \beta_t = 0,\ \omega = \beta^* = 0$ and $\delta^* = 0$.

n_1	$C_f\sqrt{Re_x}$ (CASWBNT)			$C_f\sqrt{Re_x}$ Akbar et al. [8]			$C_f\sqrt{Re_x}$ Ullah et al. [9]			$C_f\sqrt{Re_x}$ Sreenivasulu et al. [10]			$C_f\sqrt{Re_x}$ Zeb et al. [11]		
	$We = 0$	$We = 0.3$	$We = 0.5$	$We = 0$	$We = 0.3$	$We = 0.5$	$We = 0$	$We = 0.3$	$We = 0.5$	$We = 0$	$We = 0.3$	$We = 0.5$	$We = 0$	$We = 0.3$	$We = 0.5$
0.0	1.0001586	1.0001586	1.0001586	1	1	1	1	1	1	1	1	1	1.0014	1.0014	1.0014
0.1	0.9487070	0.9425107	0.9382897	0.94868	0.94248	0.93826	0.94967	0.94345	0.93922	0.94860	0.94252	0.93321	0.949674	0.943456	0.939227
0.2	0.8944786	0.8802553	0.8702879	0.89442	0.88023	0.87026	0.89509	0.88087	0.87089	0.89438	0.88019	0.87023	0.895092	0.880871	0.870891

Table 6. Comparison of CASWBNT values of $-\theta'(0)$ with those found in the published works [6, 7, 14] for different values for $Bi \to \infty$, $A_s = Ec = 0$, $n_1 = We = P = 0,\ R = \gamma_1 = l = \omega = 0,\ \theta_s = \beta^* = 0,\ \beta_v = \beta_t = 0,\ \alpha = \lambda = 0,\ \varepsilon^* = 0,\ Re_x = 0$ and $\delta^* = 0$.

Pr	Upadhya et al. [6]	Krishnamurty et al. [7]	Majeed et al. [14]	Present results (CASWBNT)
0.72	1.08762	1.088642	1.088527	1.088510828
1.0	1.33334	1.333333	1.333333	1.333332564
10	4.77582	4.796929	4.796873	4.796924924

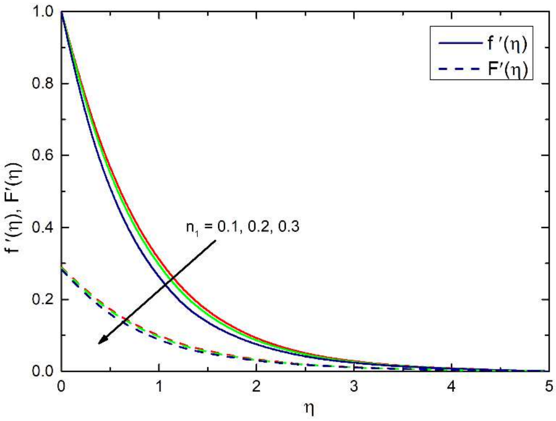

Fig. 4. $f'(\eta)$ and $F'(\eta)$ variation for n_1.

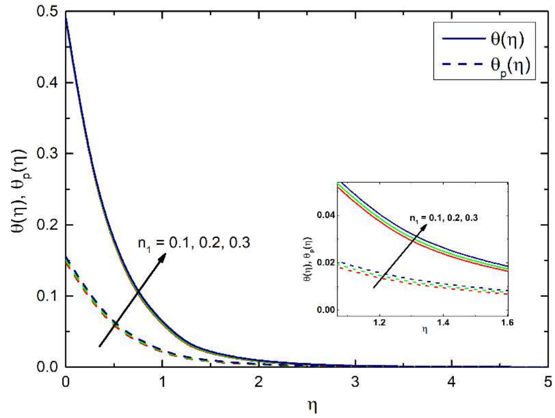

Fig. 5. $\theta(\eta)$ and $\theta_p(\eta)$ variation for n_1.

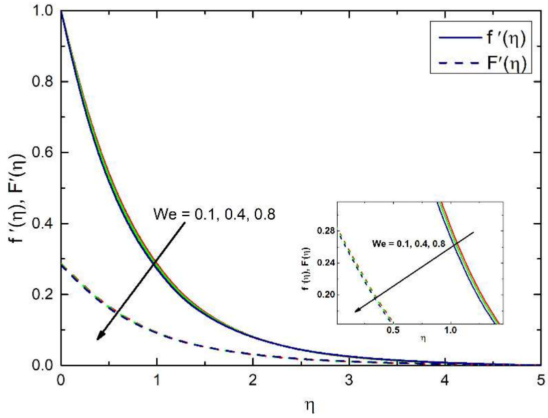

Fig. 6. $f'(\eta)$ and $F'(\eta)$ variation for We.

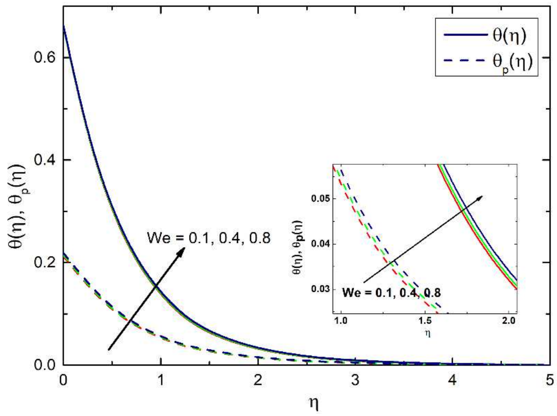

Fig. 7. $\theta(\eta)$ and $\theta_p(\eta)$ variation for We.

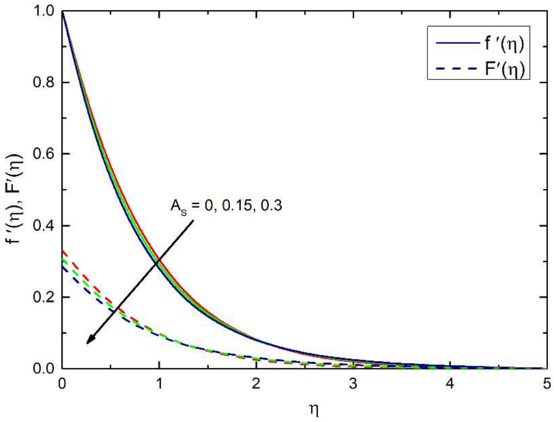

Fig. 8. $f'(\eta)$ and $F'(\eta)$ variation for A_s.

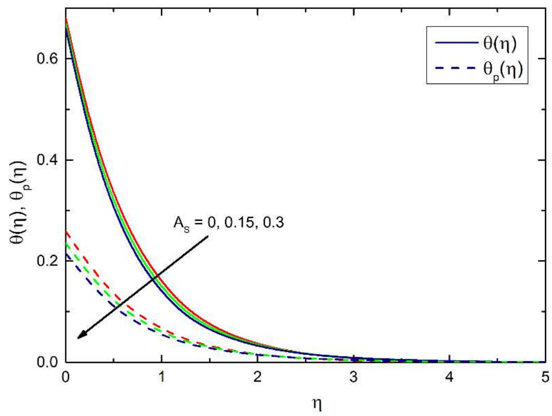

Fig. 9. $\theta(\eta)$ and $\theta_p(\eta)$ variation for A_s.

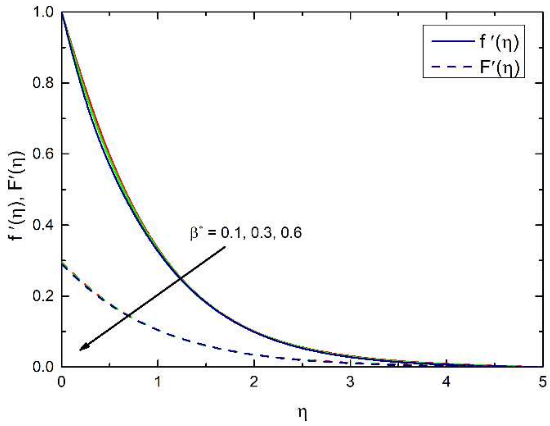

Fig. 10. $f'(\eta)$ and $F'(\eta)$ variation for β^*.

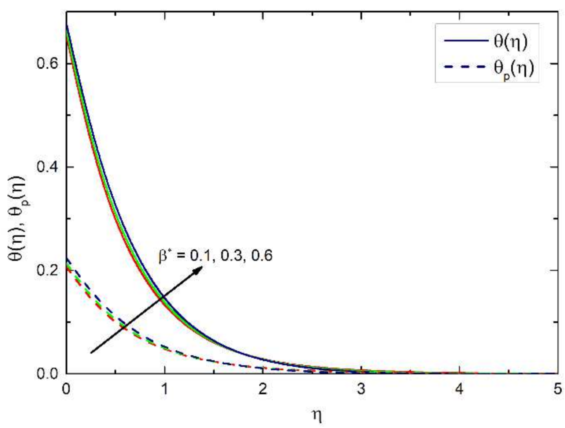

Fig. 11. $\theta(\eta)$ and $\theta_p(\eta)$ variation for β^*.

Figures 8 and 9 illustrates the velocity and thermal variation for unsteady parameter A_S. Larger A_S decreases both the velocity and thermal profile. Higher unsteadiness decreases the surface stretching rate because of high increment in time which declines the velocity. When A_S uplifts, the temperature disparity amid the stretching sheet and free stream elevates, this improves the rate of surface heat transfer, Thus, the temperature depletes. For higher unsteady parameter A_S temperature declines, that is, the cooling rate is faster. Also, cooling may require more time during steady flows. Thus, unsteady parameter contributes toward controlling the sheet temperature $\theta(0)$.

Figures 10 and 11 depict the velocity and thermal variation for ferro-hydrodynamic interaction parameter β^*. Acceleration in β^* depletes the velocity and rises the temperature. The enhancement in β^* implies the acceleration in the magnetic dipole effect. Magnetic dipole draws the fluid particles towards the surface. The fluid particles collected at the surface produces friction between them which declines the fluid velocity. The friction between the particles produces heat and hence the temperature elevates. Thus, by choosing appropriate value of the ferrohydrodynamic interaction parameter by applying an external magnetic field depending on the requirement of the thermal appliance, the rate of fluid flow and heat transfer can be managed.

Figures 12 and 13 depict the velocity and thermal attribute for diverse mixed convection parameter ω, respectively. As ω improves, the velocity escalates and thermal attribute deteriorate. The mixed convection parameter is inversely linked to the viscous force and directly correlated to the buoyancy force. With the increase in ω, the viscous force diminishes which escalates the fluid flow. Thus, the velocity accelerates. Also, ω as elevates, the buoyancy force accelerates which depletes the temperature of the fluid. Figures 14 and 15 illustrate the velocity and thermal variation for quadratic convection parameter δ^*, respectively. The velocity elevates and temperature decelerates as δ^* escalates. This is because, the quadratic term of thermal convection accelerates the thermal gradient which compels the fluid to move away from the surface. Thus, the velocity escalates. The increase in thermal gradient declines the temperature. Thus, the velocity improves and the temperature declines for higher δ^*. The mixed convection parameter and quadratic convection parameter contribute to control the rate of heat transfer.

Figures 16 and 17 portray the velocity variation and thermal distribution for various porosity parameter P, respectively. For larger P, the velocity decelerates and temperature elevates. The porosity is linked to intensive drag force and friction force. As P increases, the friction force improves which slow down fluid motion. Therefore, velocity declines. However, porosity parameter produces internal heat to the flow due to friction, this enhances in temperature of the fluid. Figures 18 and 19 demonstrate the velocity and thermal attribute variation for fluid-particle interaction parameters β_v and β_t, respectively. The enhancement of β_v depletes the velocity of fluid phase and escalates the velocity of dust phase. As β_v elevates, the dust particles require less time to change its velocity to match the fluid velocity. Thus, the velocity of dust phase improves and the velocity of fluid phase reduces as β_v increases. While the upliftment of β_t declines the temperature of the fluid phase and enhances the dust phase temperature. The elevation of fluid-particle interaction escalates the friction force in the fluid. The friction force depletes the fluid flow and improves the temperature.

Figure 20 displays the thermal distribution for various temperature ratio parameter θ_s. As θ_s enhances the thermal attribute accelerates. θ_s represents the surface temperature of the sheet. Increase in θ_s indicates improvement in surface temperature which corresponds to elevation of fluid temperature. Figure 21 describes the thermal attribute variation for radiation parameter R. For higher R, the temperature escalates. R is a source of energy which produces additional heat to working fluid. Therefore, temperature uplifts as R accelerates.

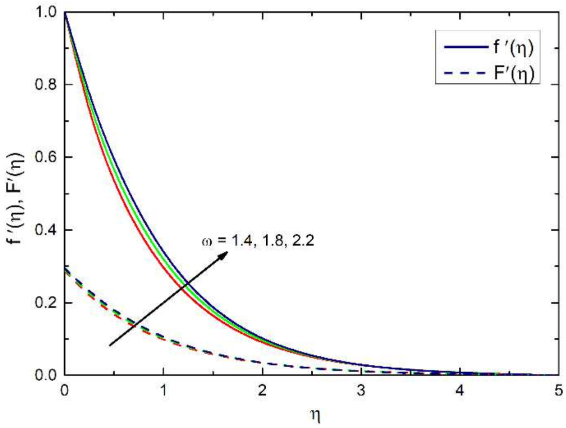

Fig. 12. $f'(\eta)$ and $F'(\eta)$ variation for ω.

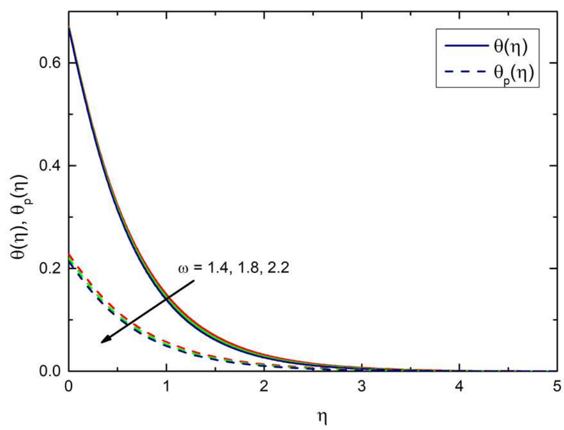

Fig. 13. $\theta(\eta)$ and $\theta_p(\eta)$ variation for ω.

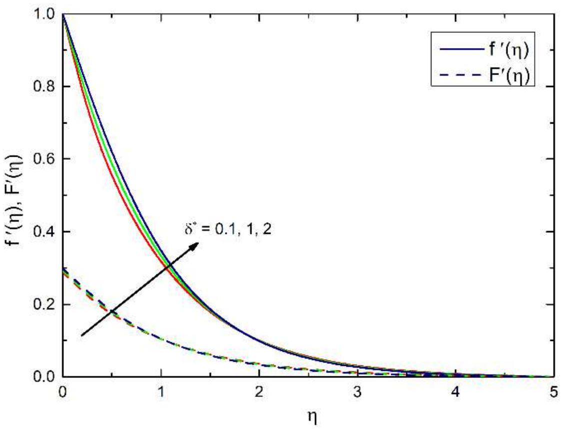

Fig. 14. $f'(\eta)$ and $F'(\eta)$ variation for δ^*.

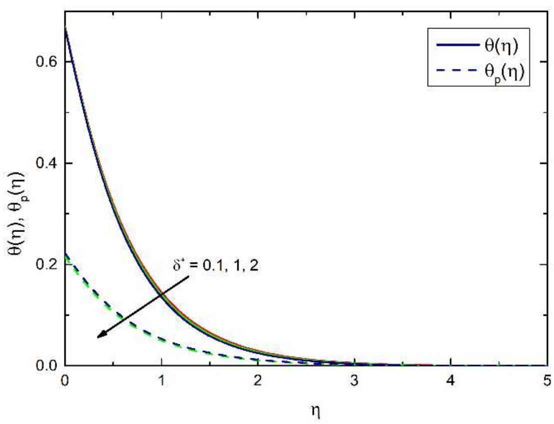

Fig. 15. $\theta(\eta)$ and $\theta_p(\eta)$ variation for δ^*.

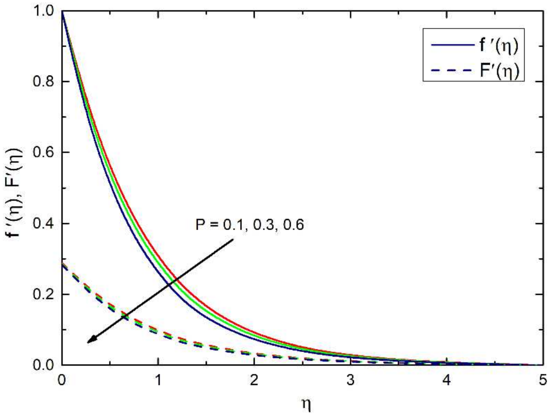

Fig. 16. $f'(\eta)$ and $F'(\eta)$ variation for P.

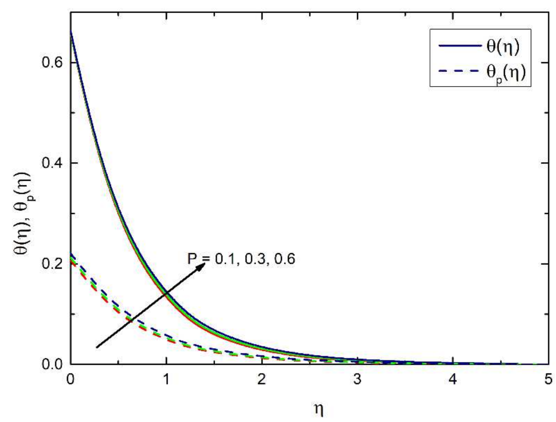

Fig. 17. $\theta(\eta)$ and $\theta_p(\eta)$ variation for P.

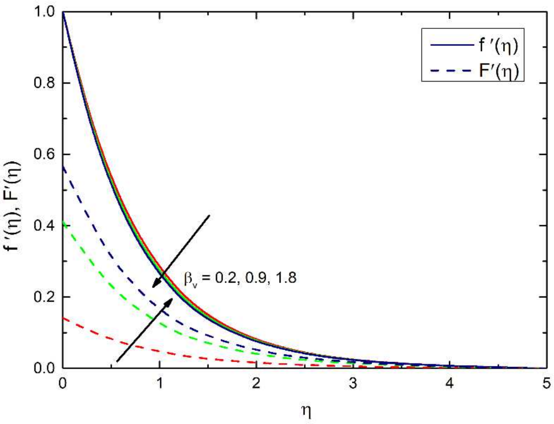

Fig. 18. $f'(\eta)$ and $F'(\eta)$ variation for β_v.

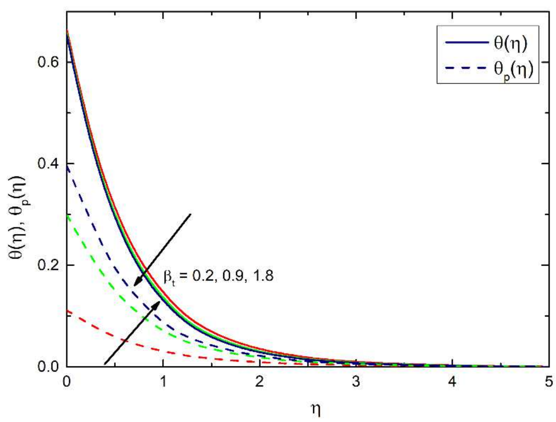

Fig. 19. $\theta(\eta)$ and $\theta_p(\eta)$ variation for β_t.

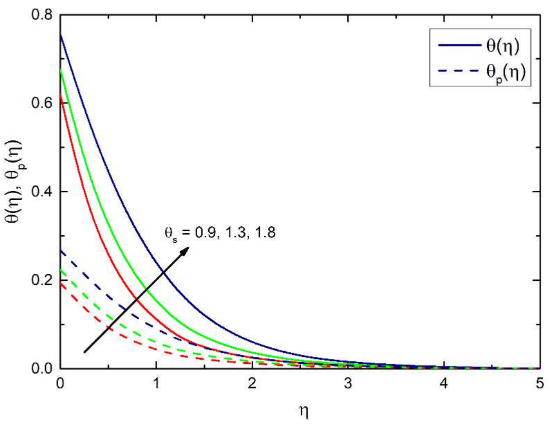

Fig. 20. $\theta(\eta)$ and $\theta_p(\eta)$ variation for θ_s.

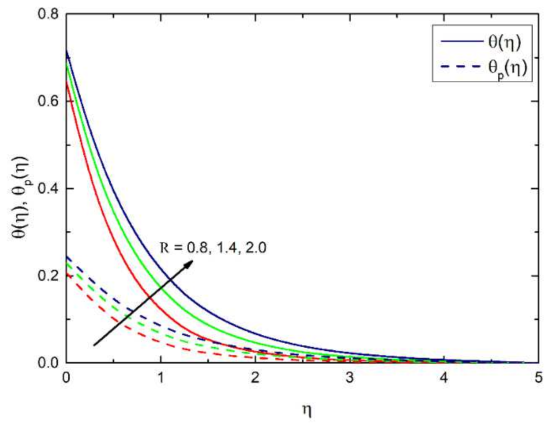

Fig. 21. $\theta(\eta)$ and $\theta_p(\eta)$ variation for R.

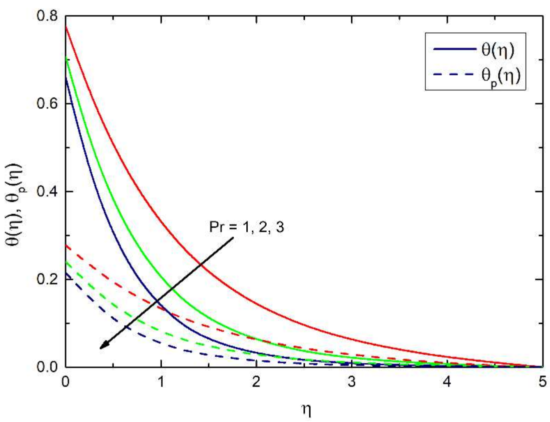

Fig. 22. $\theta(\eta)$ and $\theta_p(\eta)$ variation for Pr.

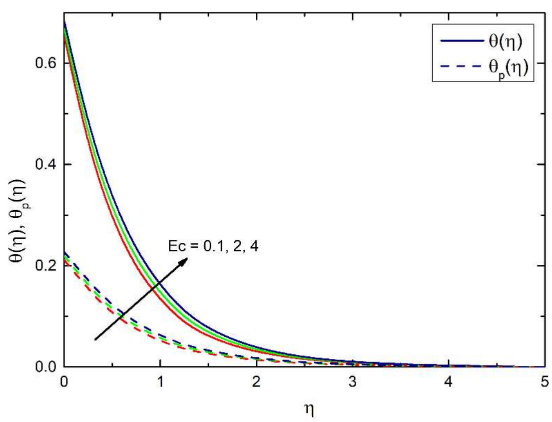

Fig. 23. $\theta(\eta)$ and $\theta_p(\eta)$ variation for Ec.

Figure 22 shows the Prandtl number Pr effect on thermal profiles. For higher Pr, the temperature depletes. Larger Pr indicates the fluid with low thermal conductivity implying the less conduction and hence temperature declines. Pr is the ratio of velocity diffusivity to heat diffusivity. Smaller Pr implies heat diffuses more quickly compared to velocity. Thus, for liquid metals, boundary layer of temperature is thicker than that of velocity. Thus, Pr is effectively used to control the relative thickness of thermal and velocity boundary layers in heat transfer process and hence cooling rate can be managed using Pr For higher Pr, the temperature drops more quickly, this implies cooling rate uplifts. Figure 23 shows the thermal attribute variation for Eckert number Ec. Thermal attribute escalates for increase in Ec. Enhancement in Ec improves the viscous dissipation that is the kinetic energy of the fluid is converted into heat energy, increase in heat energy rises the temperature of the fluid. Figure 24 depicts the Biot number Bi effect on thermal attribute. Bi is the proportion of the resistance to the heat transfer that measures the rate of convective heat transfer between fluid and sheet surface. The convective heat transfer escalates the temperature. Thus, the temperature rises as Bi accelerates.

The skin-friction coefficient $C_f\sqrt{\mathrm{Re}_x}$ and Nusselt number $Nu_x/\sqrt{\mathrm{Re}_x}$ variations are discussed graphically in Figs. 25 to 30. Figure 25 manifests the impact of Weissenberg number We and power law index n_1 on $C_f\sqrt{\mathrm{Re}_x}$. The skin-friction coefficient improves as We and n_1 escalates. Figure 26 shows the impact of fluid-particle interaction parameter for velocity β_v and mass concentration of dust particles l on $C_f\sqrt{\mathrm{Re}_x}$. As β_v and l uplifts, the skin-friction coefficient depletes. Figure 27 depicts the $C_f\sqrt{\mathrm{Re}_x}$ variation for ferro-hydrodynamic interaction parameter β^* and Prandtl number Pr. $C_f\sqrt{\mathrm{Re}_x}$ depletes for higher β^* and Pr. Figure 28 depicts the $Nu_x/\sqrt{\mathrm{Re}_x}$ variation for β^* and Pr. $Nu_x/\sqrt{\mathrm{Re}_x}$ depletes for higher β^* and improves for higher Pr.

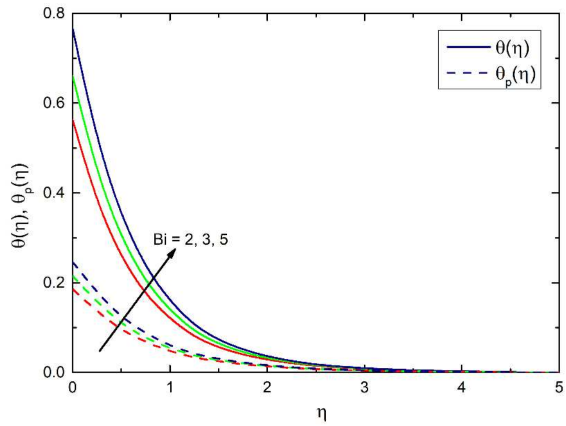

Fig. 24. $\theta(\eta)$ and $\theta_p(\eta)$ variation for Bi.

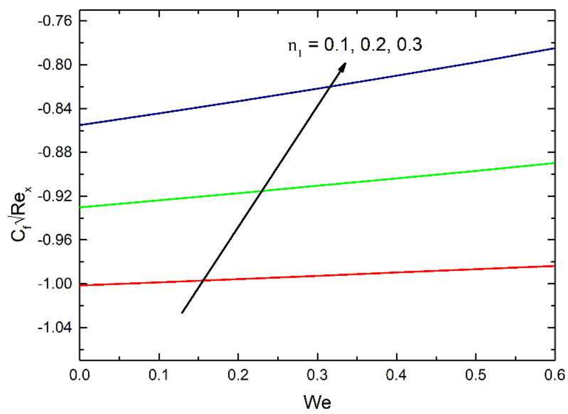

Fig. 25. Effect of We and n_1 on $C_f\sqrt{\mathrm{Re}_x}$.

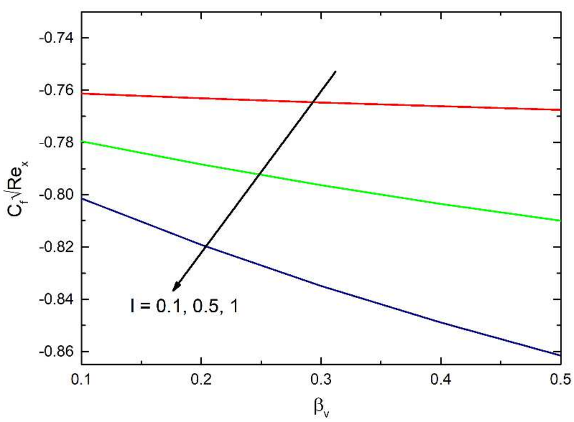

Fig. 26. Effect of β_v and l on $C_f\sqrt{\mathrm{Re}_x}$.

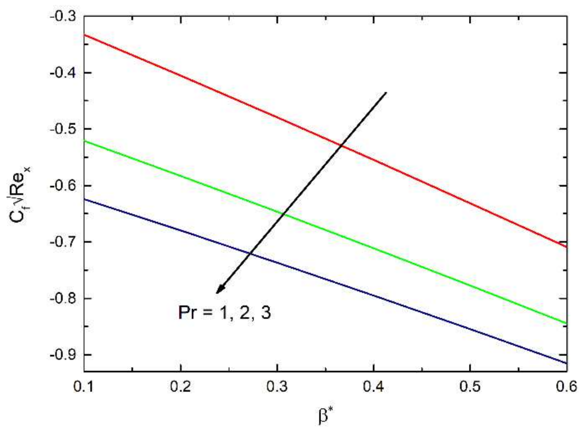

Fig. 27. Effect of β^* and Pr on $C_f\sqrt{\mathrm{Re}_x}$.

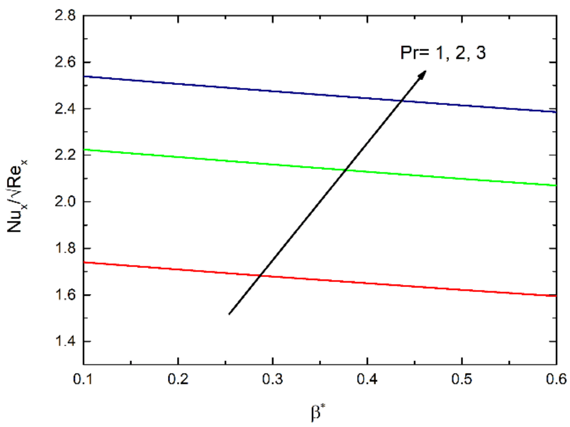

Fig. 28. Effect of β^* and Pr on $Nu_x/\sqrt{\mathrm{Re}_x}$.

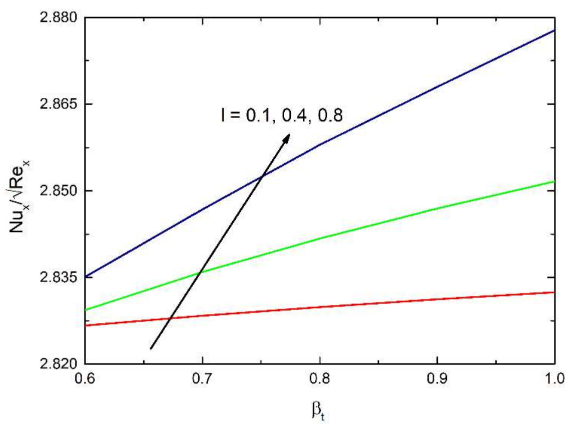

Fig. 29. Effect of β_t and l on $Nu_x/\sqrt{\mathrm{Re}_x}$.

Figure 29 demonstrates the effect of fluid-particle interaction parameter for temperature β_t and mass concentration of dust particles l on $Nu_x/\sqrt{\mathrm{Re}_x}$. The Nusselt number enhances for larger β_t and l. Figure 30 describes the influence of radiation parameter R and temperature ratio parameter θ_s on $Nu_x/\sqrt{\mathrm{Re}_x}$. As R and θ_s increase, the Nusselt number increases.

The variations of Entropy generation and Bejan number are illustrated graphically in Figs. 31 to 36. Figures 31 and 32 describe the Weissenberg number We effect on entropy generation E_{gen} and Bejan number Be, respectively. As We escalates, E_{gen} depletes and Be enhances. This is because, greater fluid thickening behaviour results in greater energy loss. Figures 33 and 34 demonstrate Brinkman Br effect on entropy generation E_{gen} and Bejan number, respectively. Improvement in Br strengthen E_{gen} and reduces Be. The Br is directly related to viscous dissipation and inversely correlated with thermal conductivity. Higher Br improves viscous dissipation which escalates the randomness and entropy generation. Larger Br implies the lower thermal conductivity, since, the viscous dissipation irreversibility dominates the heat transfer irreversibility. Thus, Be reduces for higher Br. Figures 35 and 36 illustrate the radiation parameter R effect on entropy generation E_{gen} and Bejan number Be. Acceleration of R improves E_{gen} and Be.

The skin friction co-efficient $C_f\sqrt{\mathrm{Re}_x}$ and Nusselt number $Nu_x/\sqrt{\mathrm{Re}_x}$ for various values of n_1, We, A_s, β^*, ω, δ^*, P, l, β_v, θ_s, R, Pr, Ec, β_t and Bi are illustrated in Table 7. The $C_f\sqrt{\mathrm{Re}_x}$ declines for higher Pr, A_s, β_v, β_t, l, β^* and P and uplifts for higher We, ω, δ^*, Bi, R, θ_s, Ec and n_1. $Nu_x/\sqrt{\mathrm{Re}_x}$ decreases for enhancement of l, We, n_1, β_v, β^*, P and Ec and improves for higher ω, δ^*, Pr, Bi, A_s, R, β_t and θ_s.

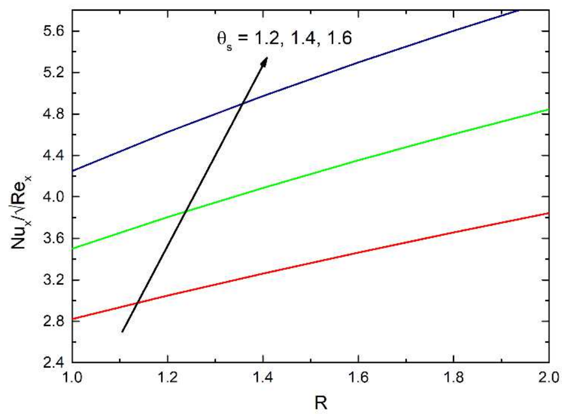

Fig. 30. Effect of R and θ_s on $Nu_x/\sqrt{\mathrm{Re}_x}$.

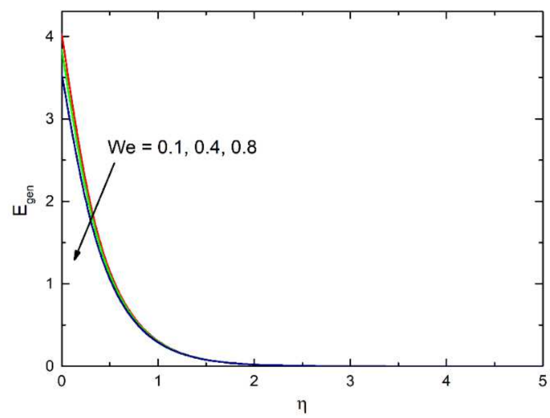

Fig. 31. E_{gen} variation for We.

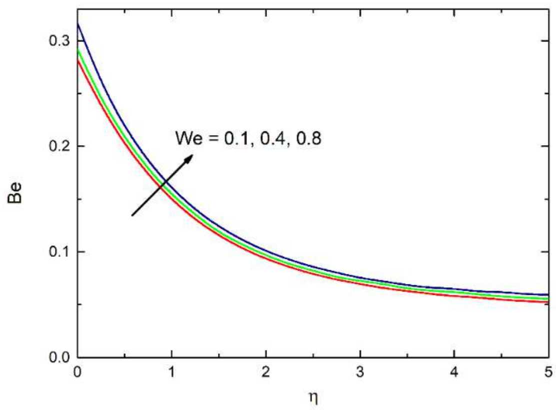

Fig. 32. Be variation for We.

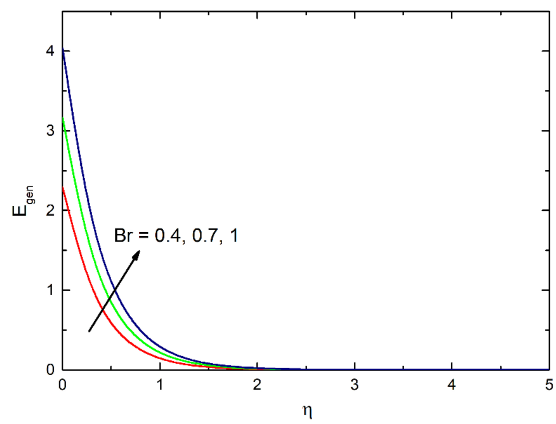

Fig. 33. E_{gen} variation for Br.

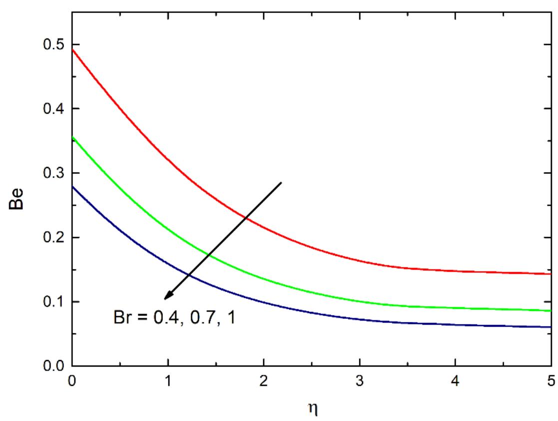

Fig. 34. Be variation for Br.

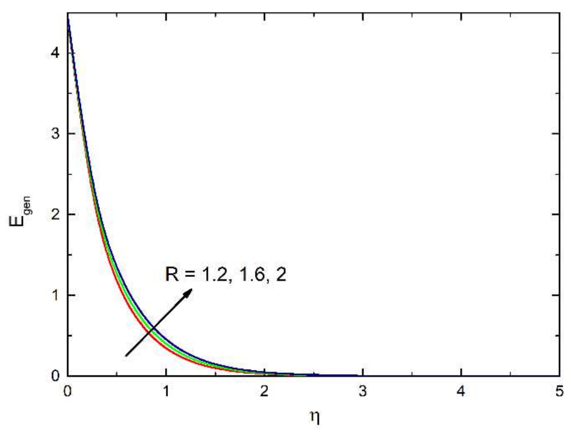

Fig. 35. E_{gen} variation for R.

Table 7. Skin friction co-efficient $C_f\sqrt{Re_x}$ and Nusselt number $Nu_x/\sqrt{Re_x}$ for diverse values of n_1, We, A_s, β^*, ω, δ^*, P, l, β_v, θ_s, R, Pr, Ec, β_t and Bi.

n_1	We	A_s	β^*	ω	δ^*	P	l	β_v	θ_s	R	Pr	Ec	β_t	Bi	$C_f\sqrt{Re_x}$	$Nu_x/\sqrt{Re_x}$
0.1	0.4	0.3	0.4	2	0.8	0.4	0.5	0.2	1.2	1	3	1	0.5	3	-0.95406738	2.45963104
0.2															-0.87780835	2.45273499
0.3															-0.79503246	2.44433745
0.3	0.1	0.3	0.4	2	0.8	0.4	0.5	0.2	1.2	1	3	1	0.5	3	-0.82270897	2.44807131
	0.3														-0.80454359	2.44564782
	0.5														-0.78518622	2.44294859
0.3	0.4	0	0.4	2	0.8	0.4	0.5	0.2	1.2	1	3	1	0.5	3	-0.73837411	2.31434706
		0.15													-0.74166285	2.38145544
		0.3													-0.69747539	2.44433745
0.3	0.4	0.3	0.1	2	0.8	0.4	0.5	0.2	1.2	1	3	1	0.5	3	-0.62417319	2.53809455
			0.3												-0.73674665	2.47492828
			0.6												-0.91531911	2.38505094
0.3	0.4	0.3	0.4	1.4	0.8	0.4	0.5	0.2	1.2	1	3	1	0.5	3	-0.94562294	2.42027760
				1.8											-0.84467242	2.43682916
				2.2											-0.74587656	2.45141109
0.3	0.4	0.3	0.4	2	0.1	0.4	0.5	0.2	1.2	1	3	1	0.5	3	-0.91341279	2.43078379
					1										-0.76168671	2.44794401
					2										-0.59768339	2.46449991
0.3	0.4	0.3	0.4	2	0.8	0.1	0.5	0.2	1.2	1	3	1	0.5	3	-0.69826018	2.46232485
						0.3									-0.76376314	2.45022486
						0.6									-0.85494199	2.43286788
0.3	0.4	0.3	0.4	2	0.8	0.4	0.1	0.2	1.2	1	3	1	0.5	3	-0.74864857	2.44849657
							0.5								-0.79503246	2.44433745
							1.0								-0.85140724	2.44286479
0.3	0.4	0.3	0.4	2	0.8	0.4	0.5	0.2	1.2	1	3	1	0.5	3	-0.77187075	2.47092583
								0.9							-0.81747487	2.43085614
								1.8							-0.84869162	2.42671284
0.3	0.4	0.3	0.4	2	0.8	0.4	0.5	0.2	0.9	1	3	1	0.5	3	-0.84008460	2.03463778
									1.3						-0.77945771	2.71612754
									1.9						-0.65911296	5.08152559
0.3	0.4	0.3	0.4	2	0.8	0.4	0.5	0.2	1.2	1.2	3	1	0.5	3	-0.77455508	2.64330567
										1.6					-0.73736073	3.01974332
										2					-0.70440508	3.37224328
0.3	0.4	0.3	0.4	2	0.8	0.4	0.5	0.2	1.2	1	1	1	0.5	3	-0.61972616	1.82454885
											2				-0.73092654	2.39619215
											3				-0.79643579	2.77730197
0.3	0.4	0.3	0.4	2	0.8	0.4	0.5	0.2	1.2	1	3	0.1	0.5	3	-0.80533853	2.49196343
												2			-0.78311890	2.39031502
												4			-0.75765653	2.27840752
0.3	0.4	0.3	0.4	2	0.8	0.4	0.5	0.2	1.2	1	3	1	0.2	3	-0.78727509	2.41387207
													0.9		-0.80126711	2.46954957
													1.8		-0.80853093	2.49972574
0.3	0.4	0.3	0.4	2	0.8	0.4	0.5	0.2	1.2	1	3	1	0.5	2	-0.84400530	2.01494803
														3	-0.79643579	2.44433745
														5	-0.73520862	2.93644332

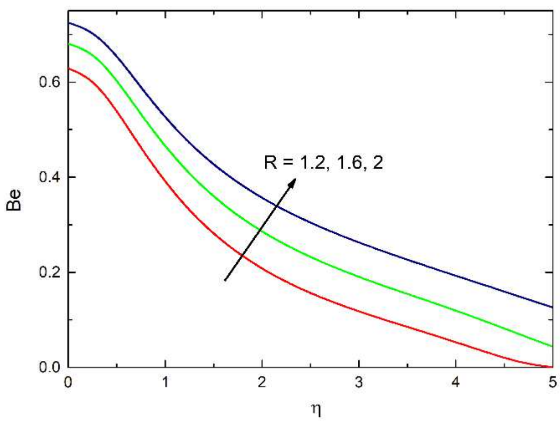

Fig. 36. *Be* variation for *R*.

7. Conclusion

The CASWBNT has been introduced to solve the set of differential equation for the analysis of an unsteady boundary layer flow and heat transfer of a dusty tangent hyperbolic fluid over a stretching sheet with magnetic dipole effect, quadratic convection, convective boundary, nonlinear radiation and entropy generation. The CASWBNT is implemented on the test problems having the exact solution, the acquired results are very near to the exact solutions in comparison to the shooting technique based RKF45 method and converges to the accuracy as the number of grid points increases. The dusty tangent hyperbolic fluid problem is solved using CASWBNT. The skin-friction coefficient for some fixed parameter obtained by CASWBNT resembles the values given in the literature. The comparisons validate the proposed technique. The impact of different factors on the velocity and thermal profile are analysed using the proposed technique and the following conclusions are drawn:

- Larger Weissenberg number and power law index parameter increases the fluid thickness due to which the velocity declines and temperature escalates. Both parameters cause a very small improvement in temperature.
- Ferro-hydrodynamic interaction and porosity parameters reduces the velocity whereas improves the temperature of the fluid. Thus, the appropriate value of Ferro-hydrodynamic interaction parameter is to be selected by applying an external magnetic field depending on the requirement of the thermal appliances in order to manage the rate of fluid flow and heat transfer.
- Mixed convection and quadratic convection parameters improve the velocity and declines the temperature. Thus, these parameters contribute to control the heat transfer rate.
- Unsteady parameter decreases both the velocity and temperature of the fluid. The unsteady parameter helps to control the temperature of the sheet.
- Fluid-particle interaction parameter reduces velocity and temperature of fluid phase whereas escalates the velocity and temperature of dust phase.
- Increasing value of Ecker number is enhancing the temperature which indicates that the more heat energy is generated in fluid due to frictional heating.
- For higher Prandtl number, the temperature decreases at a faster which implies the faster cooling rate.
- The temperature improves as Biot number escalates. Thus, the Biot number has the tendency to rise the temperature of the fluid.
- The temperature increases for temperature ratio parameter and radiation parameter.
- The Skin-friction coefficient declines for higher $\Pr, A_s, \beta_v, \beta_t, l, \beta^*$ and P and rises for higher $We, \omega, \delta^*, Bi, R, \theta_s, Ec$ and n_1. The Nusselt number decreases for higher $l, We, n_1, \beta_v, \beta^*, P$ and Ec and improves for higher $\omega, \delta^*, \Pr, Bi, A_s, R, \beta_t$ and θ_s.
- The Weissenberg number declines the E_{gen} and improves the Bejan number. Opposite trend is noticed for Brinkman number. Radiation accelerates both entropy and Bejan number.
- These results on the effect of various physical parameters on fluid flow behaviour and heat transfer are helpful for the scientists and researchers for the efficient performance of the thermal system in the emerging technologies in engineering and industrial process.

The present study is essential and provide useful information for the scientists and researchers for the efficient performance of the thermal system and for enhancing thermal management strategies and energy efficiency in many engineering, medical and industrial applications, including heat exchangers, electronic cooling, aerodynamics, NMR spectroscopy and many other.

Limitations

The results discussed in the study are valid within the framework of the present model assumptions. Any changes made to the model, equations or consideration of different physical effects may lead to deviations in the obtained results. Hence, it is important to be cautious while changing any parameters or underlying assumptions or using the results in different model.

Future Scope

The study of fluid flow behaviour and heat transfer over a stretching sheet is significant due to its vast variety of applications in engineering and industrial fields. Hence, it is important and necessary to study how to develop the correlation of flow and heat transfer. For future scope, the present study can be developed for increasing the advancements in fluid and heat transfer processes in the following ways:

- By developing the model by considering mass transfer equation.
- By modelling the energy equation using the Cattaneo–Christov heat flux model.
- By developing the model for different fluid or for different nanofluids.
- By developing the model by considering other effects like melting heat transfer, Joule heating, thermophoresis, viscous dissipation, etc.
- By developing the model for different boundary conditions and for different geometries.

Author Contributions

The main idea of this work was proposed and carried out by P.I. Kulkarni. The first draft was written by P.I. Kulkarni and all the authors commented on the first version of the manuscript. The authors S.C. Shiralashetti supervised the work. S.C. Shiralashetti and S.I. Hanaji reviewed and made some corrections in the manuscript. The manuscript was written through the contribution of all authors. All authors discussed the results, reviewed, and approved the final version of the manuscript.

Acknowledgments

We thank Karnatak University, Dharwad for the University Research Studentship (URS) during the year 2019-2020: KU/URS/2020-21/621, dated 26/10/2021 and we thank Karnataka Science and Technology Promotion Society (KSTePS), Department of Science and Technology, Government of Karnataka, No. DST/KSTePS/Ph.D. Fellowship/OTH-04:2020-21/491, Dated: 30-07-2021, for the financial support of this work.

Conflict of Interest

The authors declared no potential conflicts of interest concerning the research, authorship, and publication of this article.

Funding

The authors received no financial support for the research, authorship, and publication of this article.

Data Availability Statements

The datasets generated and/or analysed during the current study are available from the corresponding author on reasonable request.

Nomenclature

u, v	Velocity components of fluid phase in x, y direction [ms^{-1}]	T_∞	Temperature of ambient fluid [K]
u_p, v_p	Velocity components of dust particle phase in x, y direction [ms^{-1}]	R	Radiation parameter
T	Temperature of the fluid phase [K]	A_S	Unsteady parameter
a	Distance [m]	Ec	Eckert number
c_m	Specific heat of dust particles [J $kg^{-1}K^{-1}$]	H	Resultant magnetic field strength [A m^{-1}]
k'	Permeability of porous medium [m^2]	M_0	Magnetisation [A m^{-1}]
T_p	Temperature of the dust particle phase [K]	P	Porosity parameter
n_1	Power law index parameter	k^*	Mean absorption coefficient [m^{-1}]
m_1	Mass of dust particles [kg]	q_r	Radiative heat flux [Wm^{-2}]
c_p	Specific heat of fluid [J $kg^{-1}K^{-1}$]	f	Dimensionless fluid velocity
k_1	Stoke's resistance [kg m s^{-1}]	F	Dimensionless dust particle velocities
N_d	Dust particle number density	We	Weissenberg number
g	Acceleration due to gravity [ms^{-2}]	k_1^*	Pyromagnetic coefficient
k_0	Thermal conductivity [$Wm^{-1}K^{-1}$]	T_c	Curie temperature [K]
h	Heat transfer coefficient	Re_x	Local Reynolds number
U_s	Stretching velocity [ms^{-1}]	Bi	Biot number
l	Mass concentration of dust particles	Gr	Grashoff number
s	Stretching rate	E_{gen}	Dimensionless entropy generation rate
r	Unsteady factor	Br	Brinkman number
t	Time [s]	t_d	Temperature difference
Pr	Prandtl number	Be	Bejan number
T_s	Temperature of stretching surface [K]	T_f	Convective fluid temperature at the surface

Greek Symbols

ρ	Density of fluid [kg m^{-3}]	γ_1	Specific heat ratio
Γ	Time dependent material constant	τ_v	Relaxation time of fluid [s]
σ^*	Steafan-Boltzmann constant [W $m^{-2}K^{-4}$]	β^*	Ferro-hydrodynamic interaction parameter
τ_T	Thermal equilibrium time [s]	α	Dimensionless distance
δ_1, δ_2	Thermal expansion coefficient	β_v	Fluid-particle interaction parameter for velocity
μ	Co-efficient of viscosity [kg $m^{-1}s^{-1}$]	γ^*	Magnetic field strength [A m^{-1}]
τ	Extra stress tensor	ω	Mixed convection parameter
μ_∞	Infinite shear rate viscosity	δ^*	Quadratic convection parameter
μ_0	Zero shear rate viscosity	θ	Dimensionless fluid temperature
β_t	Fluid-particle interaction parameter for temperature	θ_p	Dimensionless dust particle temperature
λ	Viscous dissipation parameter	θ_s	Temperature ratio parameter
ε^*	Curie temperature ratio	$\acute{S}_{gen}$	Entropy generation rate
ρ_p	Density of dust particle [kg m^{-3}]	$\acute{S}_0$	Entropy generation characteristic
υ	Kinematic viscosity [m^2s^{-1}]		

Subscript

p	Particle phase	∞	Fluid properties at ambient condition

References

[1] Saffman, P.G., On the stability of laminar flow of a dusty gas, *Journal of Fluid Mechanics*, 13, 1962, 120-128.
[2] Shiralashetti, S.C., Kulkarni, P.I., Hanaji, S.I., Chelyshkov wavelet-based numerical technique for the solution of Darcy–Forchheimer flow of Erying–Powell radiated dusty fluid over a stretching sheet with Cattaneo–Christov heat flux, *Numerical Heat Transfer, Part B: Fundamentals,* 2024, doi: 10.1080/10407790.2024.2346933.

[3] Sulochana, C., Prakash, J., Sandeep, N., Unsteady MHD flow of a dusty nanofluid past a vertical stretching surface with non-uniform heat source/sink, *International Journal of Science and Engineering,* 10(1), 2016, 1-9.
[4] Almaneea, A., Computational investigation on transport of heat energy by flow of dusty Carreau fluid with nanoparticles using finite element method, *Ain Shams Engineering Journal,* 15, 2024, 102377.
[5] Dey, D., Makinde, O.D., Chutia, B., Hydromagnetic flow of dusty fluid with heat and mass transfer past a stretching curved surface in a porous medium, *Latin American Applied Research - An International Journal,* 52(3), 2022, 201-206.
[6] Upadhya, S.M., Mahesha, Raju, C.S.K., Shehzad, S.A., Abbasi, F.M., Flow of Eyring-Powell dusty fluid in a deferment of aluminium and ferrous oxide nanoparticles with and Cattaneo-Christov heat flux, *Powder Technology,* 340, 2018, 68-76.
[7] Krishnamurthy, M.R., Gireesha, B.J., Gorla, R.S.R., Prasannakumara, B.C., Suspended particle effect on slip flow and melting heat transfer of nanofluid over a stretching sheet embedded in a porous medium in the presence of nonlinear thermal radiation, *Journal of Nanofluids,* 5(4), 2016, 502-510.
[8] Akbar, N.S., Nadeem, S., Haq, R.U., Khan, Z.H., Numerical solutions of magneto hydrodynamic boundary layer flow of tangent hyperbolic fluid flow towards a stretching sheet with magnetic field, *Indian Journal of Physics,* 87(11), 2013, 1121-1124.
[9] Ullah, Z., Zaman, G., Ishak, A., Magnetohydrodynamic tangent hyperbolic fluid flow past a stretching sheet, *Chinese Journal of Physics,* 66, 2020, 258-268.
[10] Sreenivasulu, P., Vasu, B., Poornima, T., Reddy, N.B., Inclined Lorentzian force effect on tangent hyperbolic radiative slip flow imbedded carbon nanotubes: Lie group analysis, *Journal of Computational & Applied Research in Mechanical Engineering,* 10(1), 2020, 85-99.
[11] Zeb, S., Khan, S., Ullah, Z., Yousaf, M., Khan, I., Alshammari, N., Alam, N., Hamadneh, N. N., Lie group analysis of double diffusive MHD tangent hyperbolic fluid flow over a stretching sheet, *Mathematical Problems in Engineering,* 2022, 2022, 9919073.
[12] Moatimid, G.M., Mohamed, M.A.A., Gaber, A.A., Mostafa, D.M., Numerical analysis for tangent-hyperbolic micropolar nanofluid flow over an extending layer through a permeable medium, *Scientific Reports,* 13, 2023, 13522.
[13] Andersson, H.I., Valnes, O.A., Flow of a heated ferrofluid over a stretching sheet in the presence of a magnetic dipole, *Acta Mechanica,* 128, 1998, 39-47.
[14] Majeed, A., Zeeshan, A., Ellahi, R., Chemical reaction and heat transfer on boundary layer Maxwell Ferro-fluid flow under magnetic dipole with Soret and suction effects, *Engineering Science and Technology,* 20, 2017, 1122-1128.
[15] Nidhi, Kumar, L, Magnetic dipole and mixed convective effect on boundary layer flow of ferromagnetic micropolar hybrid nanofluid, *Journal of Nanofluids,* 13, 2024, 435-445.
[16] Kamis, N.I. Jiann, L.Y. Shafie, S. Rawi, N.A., Numerical simulation of convection hybrid ferrofluid with magnetic dipole effect on an inclined stretching sheet, *Alexandria Engineering Journal,* 76, 2023, 19-33.
[17] Tijani, Y.O., Adeosun, A.T., Ogunseye, H.A., Niranjan, H., Magnetic dipole dynamics on Reiner–Philippoff boundary layer flow, *Numerical Heat Transfer, Part A: Applications,* 85(10), 2023, 1691-1705.
[18] Imtiaz, M., Khan, M. I., Akermi, M., Hejazi, H. A., Understanding the impact of magnetic dipole and variable viscosity on nanofluid flow characteristics over a stretching surface, *Journal of Magnetism and Magnetic Materials,* 589, 2024, 171613.
[19] Goren, S.L., On free convection in water at 40 C, *Chemical Engineering Science,* 21(6-7), 1966, 515-518.
[20] Obalalu, A.M., Alfwzan, W.F., Memon, M.A., Darvesh, A., Adegbite, P., Hendy, A.S., Ali, M.R., Energy optimization of quadratic thermal convection on two-phase boundary layer flow across a moving vertical flat plate, *Case Studies in Thermal Engineering,* 55, 2024, 104073.
[21] Abbas, M. Khan, N., Hashmi, M.S., Alhefthi, R.K., Rezapour, S., Inc, M., Thermal Marangoni convection in two-phase quadratic convective flow of dusty MHD trihybrid nanofluid with non-linear heat source, *Case Studies in Thermal Engineering,* 57, 2024, 104190.
[22] Jiann, L.Y., Zin, N.A.M., Rawi, N.A., Ilias, M.R., Shafie, S., Comparative study of quadratic mixed convection MHD Carreau fluid flow on cylinder and flat plate with mass transition, *Arabian Journal for Science and Engineering,* 49, 2024, 1977-2000.
[23] Imran, M., Basit. M.A., Yasmin, S., Khan, S.A., Elagan, S.K., Akgül, A., Hassan, A.M., A proceeding to numerical study of mathematical model of bioconvective Maxwell nanofluid flow through a porous stretching surface with nield/convective boundary constraints, *Scientific Reports,* 14(1), 2024, 1873.
[24] Venkatesh, N., Raju, R.S., Anil Kumar, M., Dharmendar Reddy, Y., A numerical study on MHD Maxwell fluid with nanoparticles over a stretching surface: Impacts of thermal radiation, convective boundary condition and induced magnetic field, *Numerical Heat Transfer, Part A: Applications,* 2024, doi: 10.1080/10407782.2024.2338259.
[25] Shah, S.A.G.A., Hassan, A., Karamti, H., Alhushaybari, A., Eldin, S.M., Galal, A.M., Effect of thermal radiation on convective heat transfer in MHD boundary layer Carreau fluid with chemical reaction, *Scientific Reports,* 13, 2023, 4117
[26] Raje, A., Bhise, A.A., Kulkarni, A., Entropy analysis of the MHD Jeffrey fluid flow in an inclined porous pipe with convective boundaries, *International Journal of Thermofluids,* 17, 2023, 100275.
[27] Bejan, A., A study of entropy generation in fundamental convective heat transfer, *Journal of Heat Transfer,* 101(4), 1979, 718-725.
[28] Reddy, M.V., Vajravelu, K., Ajithkumar, M., Sucharitha, G., Lakshminarayana, P., Analysis of entropy generation and activation energy on a convective MHD Carreau–Yasuda nanofluid flow over a sheet, *Modern Physics Letters B,* 38(28), 2024, 2450266.
[29] Wang, J., Farooq, U., Waqas, H., Muhammad, T., Khan, S.A., Hendy, A.S., Ali, M.R., Numerical solution of entropy generation in nanofluid flow through a surface with thermal radiation applications, *Case Studies in Thermal Engineering,* 54, 2024, 103967.
[30] Hayat, T., Yaqoob, R., Qayyum, S., Alsaedi, A., Entropy generation optimization in nanofluid flow by variable thicked sheet, *Physica A: Statistical Mechanics and Its Applications,* 551(1), 2020, 124022.
[31] Shiralashetti, S.C., Harishkumar, E., Haar wavelet matrices for the numerical solution of system of ordinary differential equations, *Malaya Journal of Matematik,* S(1), 2020, 144-147.
[32] Shiralashetti, S.C., Badiger, P., Haar wavelet algebraic multigrid method for the numerical solution of squeeze film lubrication problem of porous journal bearings with couple stress fluid, *Palestine Journal of Mathematics,* 12(2), 2023, 578-596.
[33] Shiralashetti, S.C., Badiger, P., Chebyshev wavelets approach for the squeeze film lubrication of long porous journal bearings with couple stress fluids, *Malaya Journal of Matematik,* S(1), 2020, 138-143.
[34] Shiralashetti, S.C., Harishkumar E., Hanaji, S., Legendre wavelet operational matrix method for the analysis of thermal radiation effect on natural convection of a vertical palte embedded in a saturated porous medium, *International Journal of Ambient Energy,* 44(1), 2023, 1512-1521.
[35] Lal, S., Kumari, P., Approximation of functions with bounded derivative and solution of Riccati differential equations by Jacobi wavelet operational matrix, *Applied Mathematics and Computation,* 394, 2021, 125834.
[36] Manohara, G., Kumbinarasaiah, S., Numerical solution of a modified epidemiological model of computer viruses by using Fibonacci wavelets, *The Journal of Analysis,* 32, 2024, 529-554.
[37] Yousefi, S., Banifatemi, A., Numerical solution of Fredholm integral equations by using CAS wavelets, *Applied Mathematics and Computation,* 183(1), 2006, 458-463.
[38] Danfu, H., Xufeng, S., Numerical solution of integro-differential equations by using CAS wavelet operational matrix of integration, *Applied Mathematics and Computation,* 194(2), 2007, 460-466.
[39] Yi, M., Huang J., CAS wavelet method for solving the fractional integro-differential equation with a weakly singular kernel, *International Journal of Computer Mathematics,* 92(8), 2014, 1715-1728.
[40] Saeedi, H., Moghadam, M.M., Numerical solution of nonlinear Volterra integro-differential equations of arbitrary order by CAS wavelets, *Communications in Nonlinear Science and Numerical Simulation,* 16(3), 2011, 1216-1226.
[41] Shamooshaky, M.M., Assari, P., Adibi, H., CAS wavelet method for the numerical solution of boundary integral equations with logarithmic singular kernels, *International Journal of Mathematical Modelling Computations,* 4(4), 2024, 377-387.
[42] Saeed, U., A wavelet method for solving Caputo–Hadamard fractional differential equation, *Engineering Computations,* 39(2), 2022, 650-671.
[43] Saeed, U., A generalized CAS wavelet method for solving ψ-Caputo fractional differential equations, *Engineering Computations,* 40(6), 2023, 1351-1370.
[44] Shiralashetti, S.C., Lamani, L., CAS wavelets stochastic operational matrix of integration and its application for solving stochastic Itô-volterra integral equations, *Jordan Journal of Mathematics and Statistics,* 14(3), 2021, 555-580
[45] Bliliana, B., Roslinda, N., Numerical solution of the boundary layer flow over an exponentially stretching sheet with thermal radiation, *European Journal of Scientific Research,* 33(4), 2009, 710-717.

[46] Burden, R.L., Faires, J.D., *Numerical Analysis*, 9th Edition, Cengage Learning, Brooks/Cole, USA, 2011.
[47] Borhanifar A., Khader M.M., Jacobi operational matrix and its application for solving systems of ODEs, *Differential Equations and Dynamical Systems*, 24(4), 2016, 459-473.

ORCID iD

S.C. Shiralashetti https://orcid.org/0000-0002-0938-6953
Priyanka I. Kulkarni https://orcid.org/0000-0002-4249-0066
Savita I. Hanaji https://orcid.org/0000-0002-6006-866X

How to cite this article: Shiralashetti, S.C., Kulkarni, P.I., Hanaji, S.I. CAS Wavelet Based Numerical Technique for the Solution of Dusty Tangent Hyperbolic Fluid Flow with Magnetic Dipole Effect, Quadratic Convection and Entropy Generation, *J. Appl. Comput. Mech.*, 11(3), 2025, 585-610. https://doi.org/10.22055/jacm.2024.46918.4625